

QUALITY CONTROL AND VERIFICATION OF
DOPPLER SPECTRA COLLECTED FROM A
VERTICALLY POINTING FMCW RADAR DEPLOYED
DURING VORTEX-SOUTHEAST

by

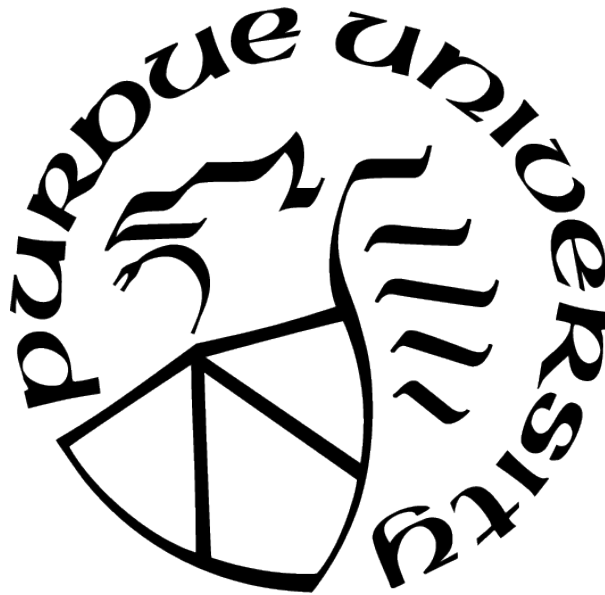
Susan Beveridge

A thesis

Submitted to the Faculty of Purdue University

In Partial Fulfillment of the Requirements for the degree of

Master of Science



Earth, Atmospheric, and Planetary Sciences

West Lafayette, Indiana

August 2021

**THE PURDUE UNIVERSITY GRADUATE SCHOOL
STATEMENT OF COMMITTEE APPROVAL**

Dr. Robin Tanamachi, Chair

Department of Earth, Atmospheric, and Planetary Sciences

Dr. Daniel Dawson

Department of Earth, Atmospheric, and Planetary Sciences

Dr. Richard Grant

Department of Agronomy

Dr. Francesc Rocabenbosch

Department of Singal Theory and Communications, Polytechnic University of
Catalonia

Approved by:

Dr. Daniel Cziczo

To my mother for always encouraging me to pursue my passion, no matter where it leads me.

ACKNOWLEDGMENTS

This work would not have been possible without support from my friends and colleagues. I first want to thank my advisor, Robin Tanamachi. I had the pleasure of meeting Robin on several occasions prior to committing to Purdue. I am grateful she saw my potential and brought me on as a member of her lab. I am especially thankful for Robin’s support and understanding amidst the COVID-19 pandemic. She quickly adapted her mentorship to a virtual setting, and extended grace and countless resources as I adapted to a new routine. Moreover, she was supportive and understanding when Connor and I uprooted our lives in West Lafayette and moved to Virginia to begin our careers while finishing our degrees remotely.

Secondly, I want to thank my labmates, Allison LaFleur and Milind Sharma. Prior to committing to Purdue, Allison befriended me and answered all my questions pertaining to graduate life at Purdue, and as a member of the Weather Radar Research Laboratory. I have also enjoyed Allison’s company as my conference travel companion. Milind helped me overcome numerous coding issues. He spearheaded coding sessions with members of Dan’s STorM Lab, and because of him, my coding experience and confidence grew.

Furthermore, this work would not be what it is today without my many collaborators. I want to thank Grant Dennany and Matt Asel for their work on transitioning the in-painting code for its application to the UMass FMCW data. Matt also helped run the in-painting method on the 2016 data set. Abhiram Gnanasambandam helped tweak parameters in the in-painting code to achieve the best results and provided clarification on the theory behind in-painting. Francesc Rocadenbosch and Joan Vilalonga provided me with the boundary layer height detection algorithm and advised me on how to receive optimal results. Andrew Pazmany provided supplemental information on coherent reflectivity factor.

A special thanks to my committee members, Daniel Dawson, Francesc Rocadenbosch, and Richard Grant. Dan spent countless hours helping with my ARPS simulations. Without his expertise, those simulations would not have been possible.

Each of my committee members provided valuable advice and feedback to enhance this work. I had many fruitful conversations with my committee, and it is evident there is much more work that could be done with the UMass FMCW observations.

Lastly, I want to thank my soon-to-be husband, Connor Belak. Thank you for following me to Purdue to pursue our master's degrees. I enjoyed every minute we spent exploring Indiana. Thank you for your support and helping keep me sane. You deserve a million thanks for debugging many of my ARPS errors and helping me run my experiments. I also want to say I am proud of you for finishing your master's degree early and landing your dream job with the National Weather Service. I cannot wait to see what the future holds for our careers as meteorologists.

This work was funded by NOAA grant NA18OAR4590313. The statements, findings, conclusions, and recommendations are those of the author(s) and do not necessarily reflect the views of the NOAA or the U.S. Department of Commerce.

TABLE OF CONTENTS

LIST OF TABLES	viii
LIST OF FIGURES	ix
ABBREVIATIONS	xii
ABSTRACT	xiv
1 INTRODUCTION	1
1.1 Motivation for VORTEX-SE	1
1.1.1 HSLC environments and cold season events	2
1.1.2 SE-US vulnerabilities	3
1.2 Motivation for this study	4
1.3 31 March 2016 case study	5
2 BACKGROUND	11
2.1 Boundary layer	11
2.1.1 Role of the boundary layer in severe convective storms	13
2.1.2 Bragg scattering	15
2.1.3 Boundary layer profiling by S-band radars	16
2.1.4 Interpreting FMCW data	17
2.2 Issues with forecasting boundary layer height	19
2.3 Data assimilation	20
2.3.1 Ensemble Kalman filter	21
3 DATA AND METHODOLOGY	23
3.1 Data	23
3.1.1 UMass FMCW observations	23
3.1.2 Spurs	25
3.1.3 Description of in-painting algorithm	25
3.1.4 Spectral power differences	31

3.1.5	Regenerating UMass FMCW moments	32
3.1.6	Boundary layer height detection algorithm	33
3.2	Numerical model	34
3.2.1	Model data	36
3.2.2	6 km simulation	37
3.2.3	3 km simulation	38
3.2.4	1 km simulation	39
4	RESULTS	40
4.1	Spectral power differences	40
4.1.1	Clear air	40
4.1.2	Precipitation	41
4.2	Moments	42
4.3	Boundary layer height detection	42
4.4	ARPS model comparison	43
5	CONCLUSIONS	60
6	REFERENCES	62

LIST OF TABLES

Table	Page
3.1 A brief description of the experiments, including the grid sizes and data assimilated.	38

LIST OF FIGURES

Figure	Page
1.1 Time-height series of reflectivity (dBZ) of clear air conditions during the overnight hours of 0400 UTC to 0500 UTC 24 March 2016. Unwanted striping caused by the spurious peaks in the Doppler spectra is evident at 1.3 km and 3.9 km. Horizon glow is located in the lowest ~ 500 m. . . .	5
1.2 Mosaic of composite reflectivity (dBZ) from 31 March 2016 for (a) early morning storms, (b) initiation of the second round, (c) mature storms, and (d) time of Priceville, AL tornado.	7
1.3 Surface analysis from the NWS Weather Prediction Center valid for 1500 UTC 31 March 2016.	8
1.4 SBCAPE (J kg^{-1} ; red contours at 100 J kg^{-1} , 250 J kg^{-1} and every 500 J kg^{-1} thereafter) and convective inhibition (CIN; J kg^{-1} ; filled blue intervals) from SPC mesoanalysis valid at (a) 1700 UTC and (b) 2200 UTC 31 March 2016.	9
1.5 0–6-km wind shear barbs (short = 5 kt, long = 10 kt) and isoshears for 40 kt, 50 kt, 60 kt from SPC mesoanalysis valid for 1900 UTC 31 March 2016. 10	
2.1 The relationships between terms used in boundary layer meteorology, as used in this thesis.	11
2.2 Conceptual diagram of the diurnal evolution of the PBL. The CBL is outlined in pink. (Adapted from Markowski and Richardson 2010.) . . .	12
2.3 Idealized boundary layer profiles of (a) daytime and (b) nighttime temperature (T ; units K), potential temperature (θ ; units K) and mixing ratio (r ; units g m^{-3}). z_i is the boundary layer height, which is taken to be the halfway point between the top of the mixed layer (residual layer) and the entrainment zone (capping inversion) during the daytime (nighttime). (Adapted from Stull 2017.)	13
2.4 Waveforms for traditional pulsed radars (top), continuous-wave radars (middle), and frequency-modulated, continuous-wave radars (bottom). (From Hegazy et al. 2016.)	17
2.5 UMass FMCW coherent reflectivity factor (dBZ) from 1200 UTC to 1300 UTC 14 March 2016. The melting layer is located at ~ 2.5 km.	18
3.1 The UMass FMCW at its 2016 VORTEX-SE deployment location near Belle Mina, AL. © Robin Tanamachi	24
3.2 Spectral profile for a clear-air case on 31 March 2016: (a) raw spectral power (in dBZ); (b) as in a, but after application of the median filter; and (c) as in a, but after application of the in-painting method.	26

Figure	Page
3.3 Flow chart of the logic for determining whether a peak in the Doppler spectra is biological or electronic in origin.	27
3.4 Simplified example of the in-painting process using a 5×5 matrix with (a) a peak in the center pixel; (b) implementation of a mask around the peak; and (c) the output image with the peak filled in according to surrounding data.	29
3.5 Example of the in-painting process for a Doppler spectral profile at 0000 UTC 31 March 2016 with (a) the raw spectral profile containing the peaks; (b) implementation of a mask around the peaks with the normalized dynamic range; and (c) the output in-painted image with the peaks filled in according to surrounding data.	31
3.6 6 km (outermost box), 3 km, and 1 km (innermost, red box) grid domains, including the locations of the WSR-88D radars that were assimilated. . .	37
3.7 A timeline of the 6 km, 3 km, and 1 km experiments. All times are in UTC.	39
4.1 Spectral profiles (a-c) as in Fig. 3.2 and spectral power differences (d-f), but for a clear air case on 14 March 2016.	46
4.2 Spectral power difference histograms for a clear air case on 14 March 2016. Panels d-f zoom in on the right tail of the distribution.	47
4.3 As in Fig. 4.1, but for precipitation on 14 March 2016.	48
4.4 As in Fig. 4.2, but for precipitation on 14 March 2016.	49
4.5 Clear air moments from 14 March 2016 that were calculated from the median filtered Doppler spectra (a-d) and in-painted Doppler spectra (e-h).	50
4.6 As in Fig. 4.5, but for precipitation on 14 March 2016.	51
4.7 Reflectivity (in dBZ) from UMass FMCW observations taken during the 2016 VORTEX-Southeast field campaign. (From Tanamachi et al. 2019.)	52
4.8 Coherent reflectivity (in dBZ) from UMass FMCW observations taken during the 2016 VORTEX-SE field campaign.	53
4.9 Boundary layer height detection algorithm for a clear-air CBL on 31 March 2016 for (a) median filtered reflectivity factor and (b) in-painted coherent reflectivity factor.	54
4.10 PBL height histograms for select clear air CBLs in March 2016 using (a) median filtered moments and (b) in-painted moments. The red line denotes the height of a known, persistent, high-power spur at 1.3 km (Figs. 1.1 and 4.7).	54

Figure	Page
4.11 Time series of PBL depth from 1800 UTC 31 March 2016 to 0100 UTC 01 April 2016 for forecast PBL depth near Belle Mina, Alabama from the 40 ARPS ensemble members (gray), ARPS ensemble mean (blue), and UMass FMCW observations (red).	55
4.12 UMass FMCW boundary layer height retrievals (pink dots) from the Lange et al. (2015) algorithm for 1700 UTC to 0200 UTC 31 March 2016. Note that this time series is also plotted in red in Fig. 4.11.	56
4.13 Time series of ensemble mean potential temperature from 1800 UTC 31 March 2016 to 0100 UTC 1 April 2016 near Belle Mina, Alabama from the ARPS model.	57
4.14 Skew-T, log p plot of ARPS model soundings (for ensemble member 1) before and after the boundary layer stabilization on 31 March 2016. Sounding values plotted are temperature (red line) and dew point temperature (blue line) at 2200 UTC, and temperature (magenta line) and dew point temperature (cyan line) at 2330 UTC. Note the warming and drying over the 900 hPa to 800 hPa layer between 2200 UTC and 2330 UTC.	58
4.15 ARPS model ensemble mean vertical velocity (w) (blue line) from 2200 UTC to 2330 UTC 31 March 2016. Positive (negative) velocities correspond to upward (downward) motion.	59

ABBREVIATIONS

ABL	atmospheric boundary layer
ADMM	alternating direction method of multipliers
ARL	above radar level
ARPS	Advanced Regional Prediction System
ASOS	Automated Surface Observing System
CAPE	convective available potential energy
CBL	convective boundary layer
CP	coherent power
DA	data assimilation
(E)F	(Enhanced) Fujita
EKF	extended Kalman filter
EnKF	ensemble Kalman filter
EOL	Earth Observing Laboratory
FAR	false alarm ratio
FMCW	frequency-modulated, continuous-wave
HS HC	high-shear, high-convective available potential energy
HS LC	high-shear, low-convective available potential energy
IOP	Intensive Observing Period
LCL	lifted condensation level
LFC	level of free convection
MIRSL	Microwave Remote Sensing Laboratory
NAM	North American Mesoscale Forecast System
NOAA	National Oceanic and Atmospheric Administration
NWP	numerical weather prediction
NWS	National Weather Service
PBL	planetary boundary layer
POD	probability of detection
SE-US	Southeast United States

SNC	coherent signal to noise ratio
SNR	signal to noise ratio
SPC	Storm Prediction Center
SRH	storm relative helicity
UMass	University of Massachusetts
U.S.	United States
UTC	Coordinated Universal Time
VORTEX-SE	Verification of the Origins of Rotation in Tornadoes Experiment- Southeast
WSR-88D	Weather Surveillance Radar-1988 Doppler

ABSTRACT

The University of Massachusetts S-band frequency-modulated, continuous-wave radar (UMass FMCW) was deployed to monitor the growth of the convective boundary layer over northern Alabama during the Verification of the Origins of Rotation in Tornadoes Experiment-Southeast (VORTEX-SE). The Doppler spectra collected in 2016 from the vertically-pointing UMass FMCW contain “spurs”, or spurious spectral peaks, caused by high-voltage switching power supplies in the traveling wave tube amplifier. In the original data processing scheme for this radar, a median filtering method was used to eliminate most of the spurs, but the largest ones persisted, which significantly degraded the quality of derived radar moments (e.g., reflectivity, Doppler velocity, and spectrum width) and hindered further analysis of these data (e.g., boundary layer height tracking).

In this study, a novel “in-painting” image processing technique was applied to remove the spurs in the Doppler spectra. We hypothesized the in-painting method would exhibit superior performance to the median filter at removing large spectral peaks, and also improve downstream radar products derived from the spectra. First, a Laplacian filter identified and masked spikes in the spectra that were characteristic of the spurs in shape and amplitude. The in-painting method then filled in masked areas based on surrounding data. Via a histogram analysis, the in-painting method was found to be more effective than the median filter at removing the large spurs from the Doppler spectra. The radar moments were then recomputed using a coherent power (CP) technique, resulting in cleaner reflectivity, Doppler velocity, and spectrum width data. Improvement was also found downstream when a boundary layer height detection algorithm was applied to the moments generated from the in-painted spectra. Output from the boundary layer height detection algorithm was then used to verify forecast boundary layer height from the Advanced Regional Prediction System (ARPS) model for the 31 March 2016 VORTEX-SE tornadic case study.

1. INTRODUCTION

1.1 Motivation for VORTEX-SE

For decades, the central and southern Great Plains region has been the epicenter of meteorological data collection related to severe weather, and for good reason. Researchers and storm chasers target this area due to the high density and visibility of severe weather events, including tornadoes. Accordingly, this region of the United States (U.S.) has been termed “Tornado Alley.” However, in recent years there has been an increasing number of severe weather outbreaks in the southeast region of the U.S. (hereafter SE-US) (e.g., Dixon et al. 2011; Agee et al. 2016; Gensini and Brooks 2018). For example, Fig. 5 in Gensini and Brooks 2018 shows a decrease in gridded tornado reports in the central and southern Plains and an increase in reports in the SE-US. A relative paucity of severe weather observations from the SE-US was a main driver behind the Verification of the Origins of Rotation in Tornadoes Experiment-Southeast (VORTEX-SE) field campaign, which took place during Spring 2016, Spring 2017, and Spring 2018.

There are known differences between tornadic storms in the SE-US and Great Plains, including differences in thermal and moisture profiles (Rasmussen 2015; Anderson-Frey et al. 2019). Convective available potential energy (CAPE) quantifies the amount of energy available for convection and typically, the larger the CAPE value, the greater the potential for severe weather (Branick 1996). Vertical wind shear, hereafter denoted only as “shear”, is a change in wind speed and/or direction with height (Markowski and Richardson 2010). Storms in the SE-US tend to be characterized by high-shear, low-CAPE (HSLC) environments (Sherburn and Parker 2014), whereas storms in the Great Plains commonly form in high-shear, high-CAPE (HSHC) environments (Thompson et al. 2004; Schneider et al. 2006). Furthermore, many SE-US tornadoes occur during the cool season (e.g., Burke and Schultz 2004; Guyer et al. 2006; Smith et al. 2008; Davis and Parker 2014; Sherburn and Parker 2014) and at night (e.g., Kis and Straka 2010; Davis and Parker 2014; Sherburn and Parker 2014; Anderson-Frey et al. 2019). The societal impacts of tornadoes in these

regions also vary, with the SE-US having greater population density and more frequent inferior building structure compared to the Great Plains (e.g., Ashley et al. 2008; Strader et al. 2017; Strader and Ashley 2018).

1.1.1 HSLC environments and cold season events

HSLC environments are commonly defined as having surface-based (SB) and mixed layer (ML) $\text{CAPE} \leq 500 \text{ J kg}^{-1}$ (Guyer and Dean 2010), most unstable parcel (MU) $\text{CAPE} \leq 1000 \text{ J kg}^{-1}$, and 0–6-km shear vector magnitude $\geq 18 \text{ m s}^{-1}$ (Sherburn and Parker 2014). While these conditions can be satisfied across all regions of the U.S. during any time of day and year (Sherburn and Parker 2014), they are most prevalent in the SE-US (Schneider et al. 2006; Sherburn and Parker 2014) during the cool season (e.g., Burke and Schultz 2004; Guyer et al. 2006; Smith et al. 2008; Davis and Parker 2014; Sherburn and Parker 2014) and overnight hours (e.g., Kis and Straka 2010; Davis and Parker 2014; Sherburn and Parker 2014; Anderson-Frey et al. 2019).

HSLC environments occur frequently, but produce severe weather only a small percentage of the time, creating a challenge for forecasters (Sherburn and Parker 2014). Storms that form in these environments tend to be horizontally and vertically smaller than traditional HSHC storms of the Great Plains (Davis and Parker 2014). These storms may be poorly sampled by the Weather Surveillance Radar 1988-Doppler (WSR-88D) network, with small-scale and low-altitude circulations poorly resolved, especially with increasing distance from the radar (Davis and Parker 2014). Furthermore, traditional forecasting techniques (Johns and Doswell 1992) have been shown to not perform as well in HSLC environments (Sherburn and Parker 2014), resulting in greater uncertainty and consequently, higher false alarm ratios (FAR) and reduced probability of detection (POD) (Guyer and Dean 2010). Additional complexities arise because high intensity tornadoes (rated 2+ on the Fujita (F) and Enhanced Fujita (EF) scales) (NOAA 2007) have been associated with a variety of storm modes in HSLC environments (Przybylinski 1995).

Guyer and Dean (2010) performed an extensive study on tornadoes in low-CAPE environments. They found that mid-level (700-500 mb) and low-level (0-3 km) lapse rates in low-CAPE environments were lower than in environments with greater buoyancy (Guyer and Dean 2010). They attributed this to the lack of an elevated mixed layer due to increased moisture and/or cool season environments (Guyer and Dean 2010). Additionally, low-CAPE tornadoes were associated with lower surface temperatures and dewpoints, as well as higher low-level relative humidity and lower lifted condensation levels (LCLs) (Guyer and Dean 2010). HSLC environments of the SE-US account for more significant tornadoes than their Great Plains HSHC counterparts (Sherburn and Parker 2014). According to Guyer and Dean (2010), more than half of the low-CAPE tornadoes had MLCAPE values $\leq 250 \text{ J kg}^{-1}$, and of all low-CAPE tornadoes, 7.7% were significant (E)F2-(E)F5.

1.1.2 SE-US vulnerabilities

There are a multitude of factors that make the population of the SE-US exceptionally vulnerable to tornadoes. Alabama has the greatest number of low-CAPE tornadoes, as well as the greatest number of (E)F2+ low-CAPE tornadoes (Guyer and Dean 2010). Forested land cover, hilly topography, and low cloud bases make it difficult to visually identify tornadoes in the SE-US (Ashley et al. 2008; Brotzge and Erickson 2010). Moreover, tornadoes occurring in the region extending from Texas eastward through Florida are most frequent during the climatological minimum in annual U.S. tornado activity from November to April (Ashley et al. 2008; Guyer and Dean 2010).

The SE-US also has one of the highest nocturnal tornado percentages (Ashley et al. 2008). According to Brotzge and Erickson (2010), tornadoes that occur overnight have a greater likelihood of being unwarned compared to those that occur during the afternoon hours. Additionally, “tornadoes at night are almost twice as likely to kill than those during the daytime” (Ashley et al. 2008). This is in part because tornadoes are more difficult to visually identify at night and the public may not receive the warning if they are asleep (Ashley et al. 2008). The public also tends to

be in more vulnerable building structures (e.g., mobile or “manufactured” and single-family homes) at night compared to steel or reinforced concrete buildings, such as schools or workplaces, during the day (e.g., Simmons and Sutter 2005; Ashley 2007; Strader et al. 2017; Strader and Ashley 2018). The SE-US has some of the largest populations living in mobile homes in the U.S., and 44.8% of all tornado deaths occur in mobile homes (Ashley et al. 2008). Furthermore, tornado sirens are designed to alert people who are outdoors and thus, are less effective at alerting the public during nocturnal tornadoes when most people are indoors (Ashley et al. 2008).

1.2 Motivation for this study

Because of the above factors, the SE-US sees a disproportionate share of tornado fatalities. Furthermore, climatological studies suggest this region will experience more frequent tornado environments in the future (Dixon et al. 2011; Agee et al. 2016; Li and Chavas 2021). VORTEX-SE was initiated to investigate SE-US tornadoes, their environments, and their societal impacts (Koch 2016; Rasmussen and Koch 2016). Different branches (i.e., physical science, operations, and social science) were tasked with one of the aforementioned objectives. This study falls within the physical science realm. Differences between the SE-US and Great Plains environments have implications on the growth and evolution of the planetary boundary layer (PBL), which in turn, affects the atmosphere’s ability to generate and sustain severe thunderstorms. Accordingly, some objectives of VORTEX-SE included examining the nocturnal boundary layer, the maintenance of large PBL vertical shear, and rapid destabilization of the PBL (Rasmussen 2015). During VORTEX-SE, the University of Massachusetts Amherst S-band frequency-modulated, continuous-wave radar (hereafter, UMass FMCW; described in more detail in the Methodology section) was deployed to monitor the growth of the convective boundary layer (CBL) over northern Alabama. The objective of this deployment was to collect high-temporal resolutions of the boundary layer structure over northern Alabama, and predict the timing of destabilization and convective initiation.

Unfortunately, the Doppler spectra collected during the 2016 VORTEX-SE campaign contain spurious peaks, resulting in unwanted striping in the derived radar moments (Fig. 1.1). Furthermore, effects from receiver saturation, which we termed "horizon glow," masked details in the CBL (Fig. 1.1). Therefore, *this thesis describes a unique data quality issue affecting UMass FMCW Doppler spectra, and a novel solution (combining an image processing technique and a signal processing technique) that allowed much of the underlying information to be recovered. It is hypothesized the novel combination of image processing and signal processing techniques will outperform traditional methods and improve downstream products.*

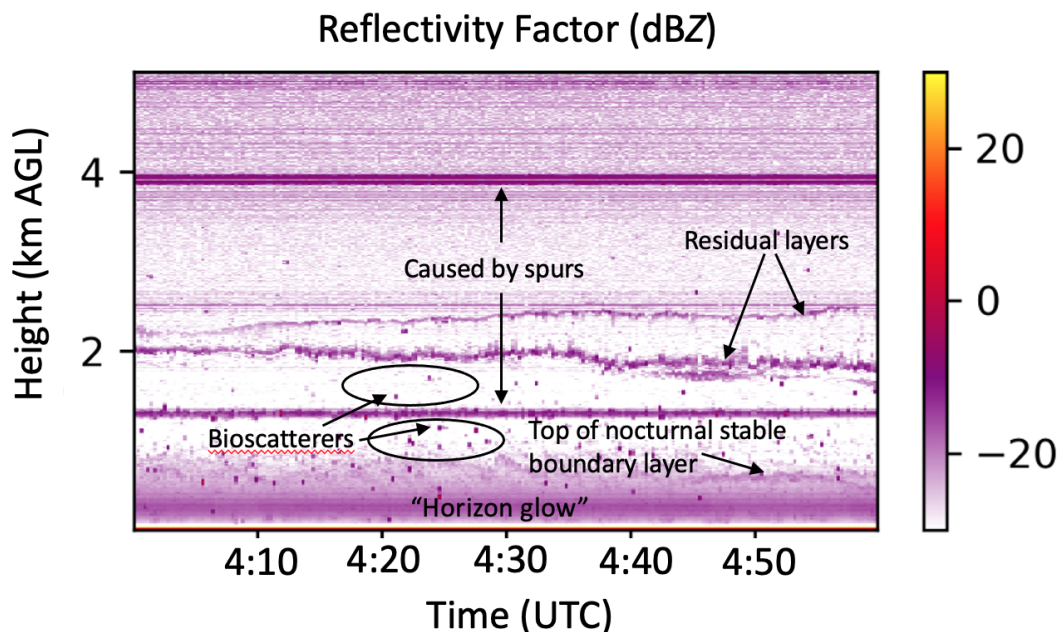


Figure 1.1. Time-height series of reflectivity (dBZ) of clear air conditions during the overnight hours of 0400 UTC to 0500 UTC 24 March 2016. Unwanted striping caused by the spurious peaks in the Doppler spectra is evident at 1.3 km and 3.9 km. Horizon glow is located in the lowest ~ 500 m.

1.3 31 March 2016 case study

The 2016 VORTEX-SE observational field campaign, which UMass FMCW was a part of, lasted several weeks. When severe weather was anticipated, Intensive Observ-

ing Periods (IOPs) were declared in which specialized observations (i.e. supplemental radar deployments, radiosondes, surface observations, etc.) were collected. The environmental setup on 31 March 2016 prompted VORTEX-SE IOP3, as this was the third IOP during the 2016 field campaign. During the early morning of 31 March 2016, there was a round of widespread, non-severe convection across the VORTEX-SE domain associated with a mesoscale convective system that moved through Tennessee and Alabama (Fig. 1.2a). The rain and cool outflow from the morning convection stabilized the boundary layer. However, rapid destabilization from direct insolation and near-surface moisture advection was expected to take place in the afternoon, creating an environment supportive of supercells (LaFleur et al. 2018).

The potential for evening convection was associated with an upper-level trough moving eastward from the Rocky Mountains and a surface low pressure system situated near the Great Lakes, with a cold front extending south into eastern Texas and progressing eastward (Fig. 1.3). Southerly surface winds advected warm, moist air northward from the Gulf of Mexico. The 1700 UTC Storm Prediction Center (SPC) mesoscale analysis (mesoanalysis) showed $< 100 \text{ J kg}^{-1}$ SBCAPE in northern Alabama (Fig. 1.4a). Around this time, the CBL began to redevelop. Over the next several hours, SBCAPE values increased to $> 1000 \text{ J kg}^{-1}$ (Fig. 1.4b) (LaFleur et al. 2018). Around 1900 UTC, isolated storms began to initiate in north central Mississippi and rapidly translate northeast (Fig. 1.2b). Westerly 0–6-km shear ranged from 40–60 kt from north central Mississippi to north central Alabama (Fig. 1.5).

Just before 2200 UTC, the National Weather Service (NWS) SPC released a Mesoscale Discussion (#311) regarding the severe potential for these storms and their environment (NWS Storm Prediction Center 2016). In their discussion, the forecasters mentioned a large residual outflow boundary across north central Alabama from the morning convection. This boundary aided in generating 0–1-km storm relative helicity (SRH) values around $+200 \text{ m}^2 \text{ s}^{-2}$. At 2300 UTC, a tornado watch (#72) was issued for west central and northern Alabama (NWS Storm Prediction Center 2016). As the storms progressed, the convective mode became a mixture of discrete supercells and multi-cell clusters (Fig. 1.2c). With an environment characterized by

backing winds, ample SRH, and warm air advection, the storms continued to exhibit low-level rotation over the next several hours as they entered the VORTEX-SE domain. At 0154 UTC, a tornado rated EF-2 on the EF scale was produced in Morgan County, Alabama near Priceville (Fig. 1.2d). Shortly afterward, the storms exited the Huntsville domain and VORTEX-SE field operations concluded for the day.

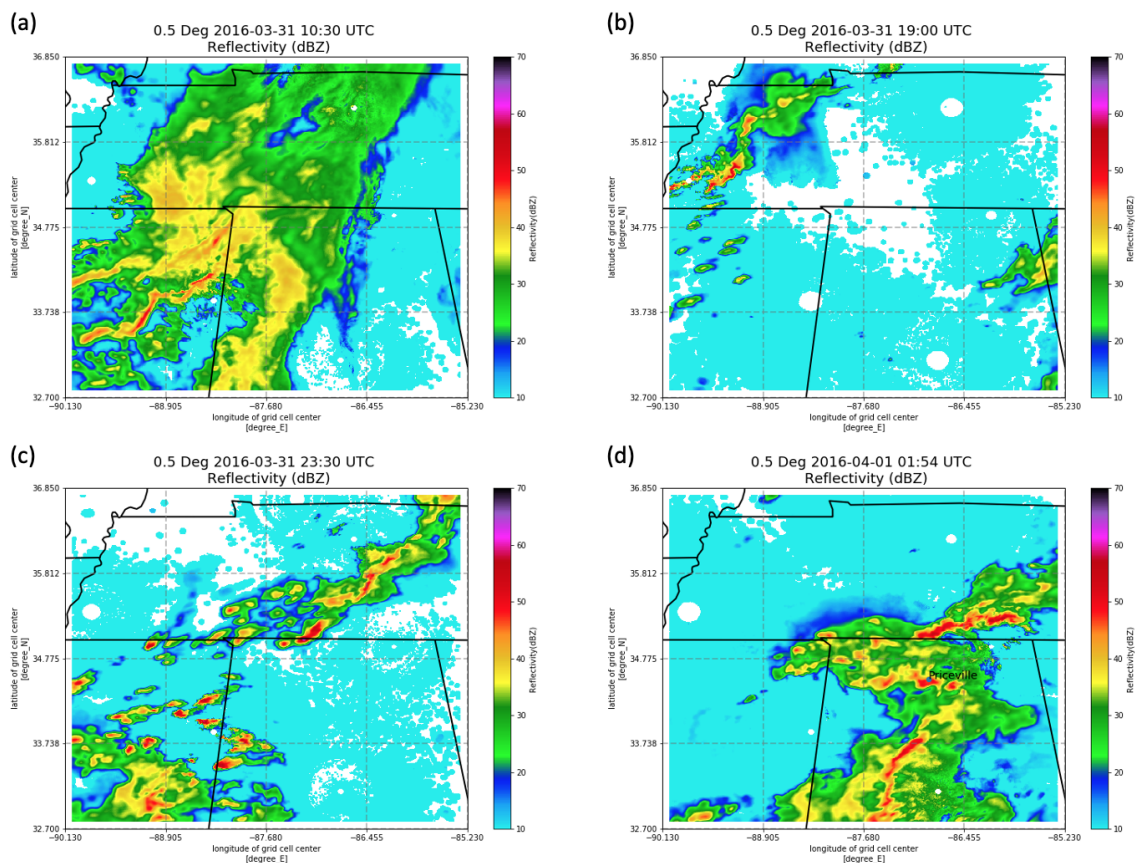


Figure 1.2. Mosaic of composite reflectivity (dBZ) from 31 March 2016 for (a) early morning storms, (b) initiation of the second round, (c) mature storms, and (d) time of Priceville, AL tornado.

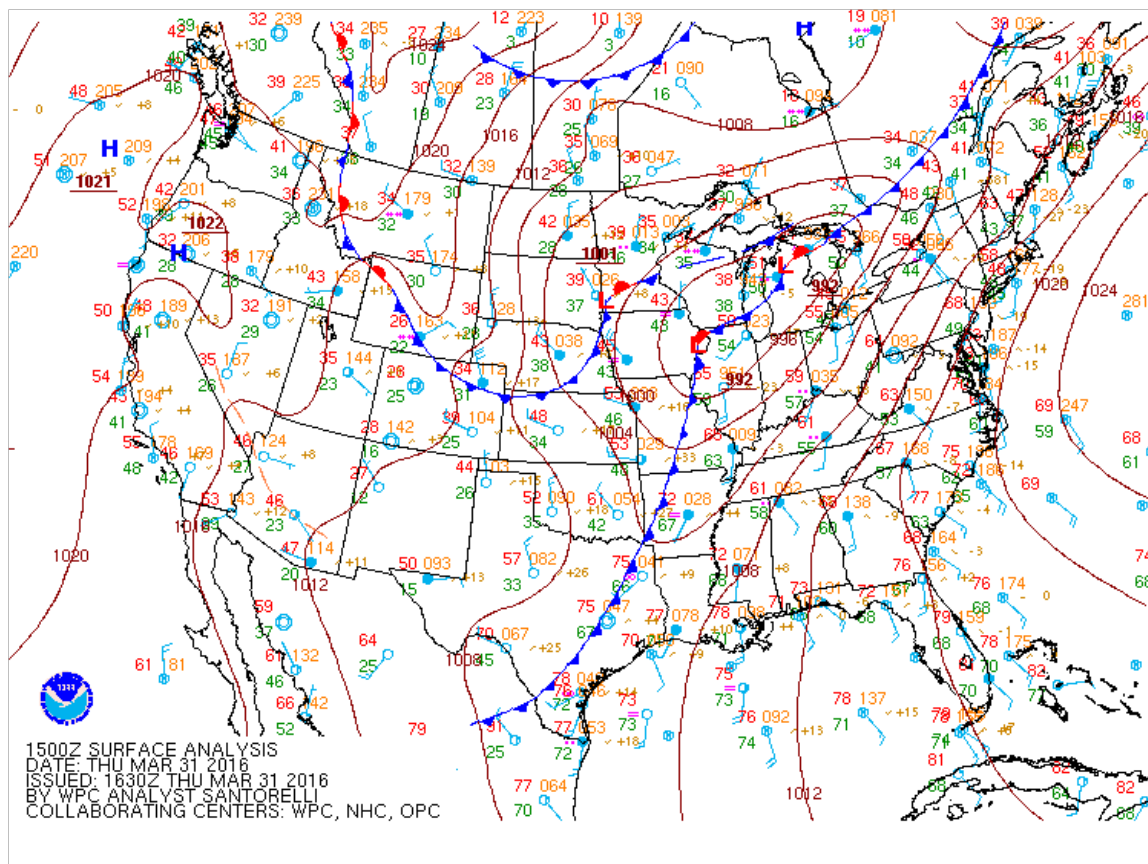


Figure 1.3. Surface analysis from the NWS Weather Prediction Center valid for 1500 UTC 31 March 2016.

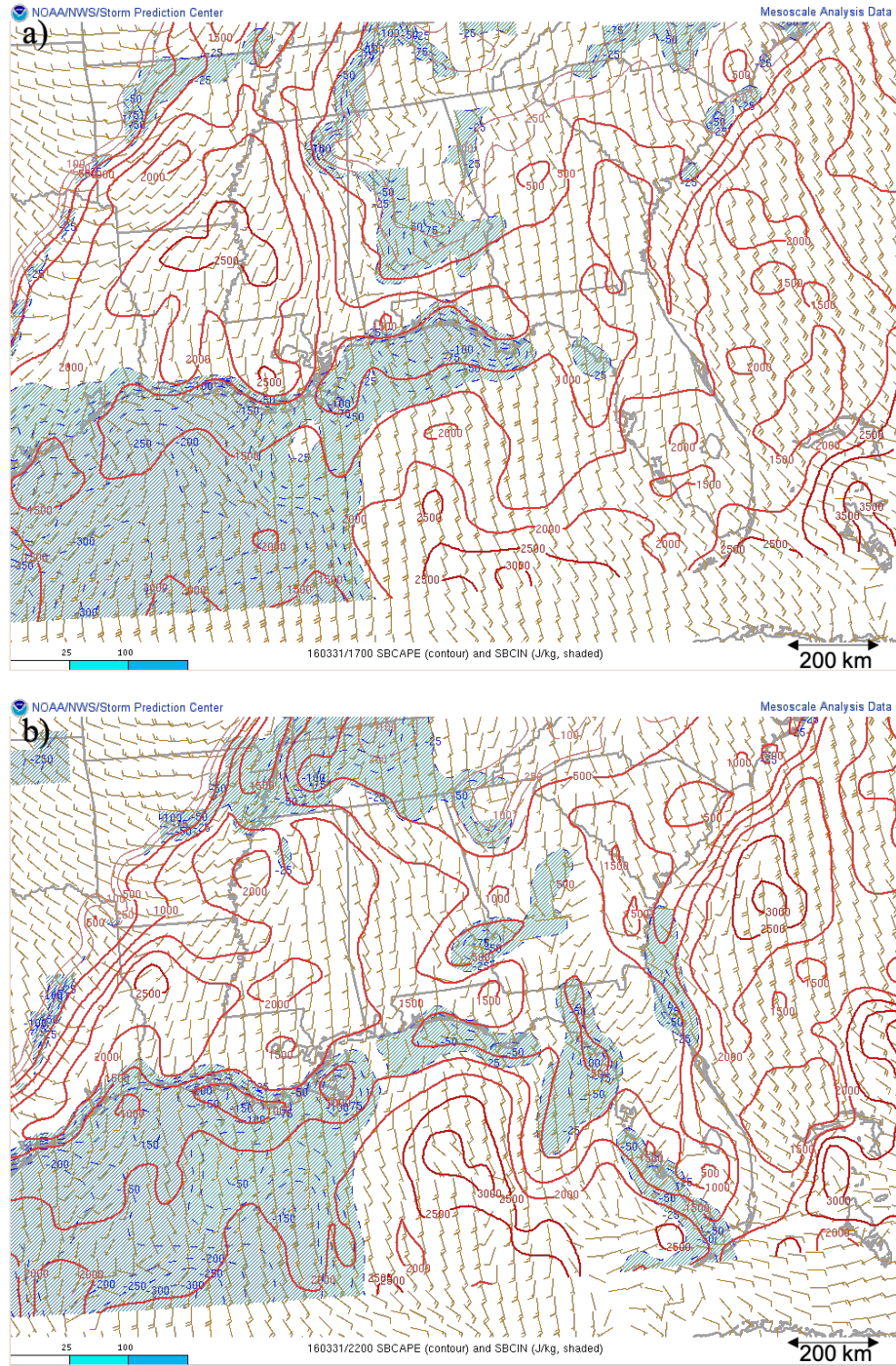


Figure 1.4. SBCAPE (J kg^{-1} ; red contours at 100 J kg^{-1} , 250 J kg^{-1} and every 500 J kg^{-1} thereafter) and convective inhibition (CIN; J kg^{-1} ; filled blue intervals) from SPC mesoanalysis valid at (a) 1700 UTC and (b) 2200 UTC 31 March 2016.

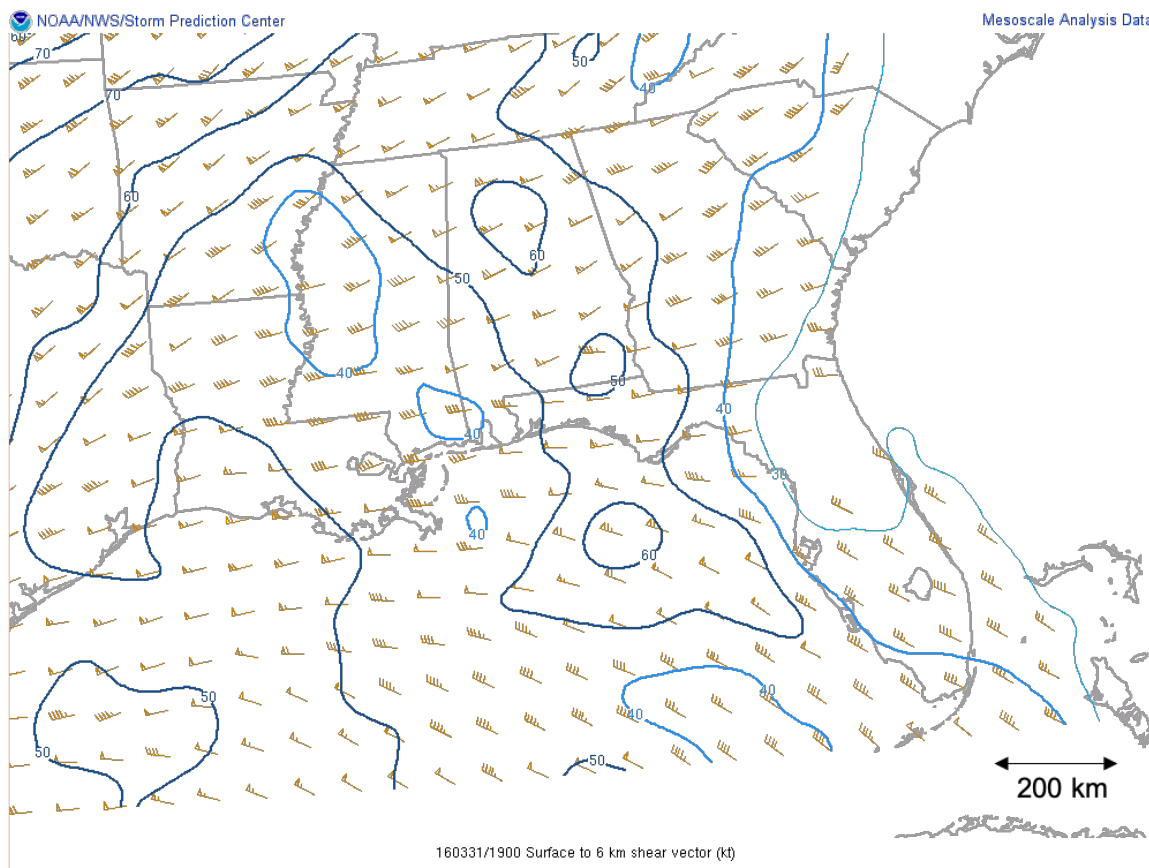


Figure 1.5. 0–6-km wind shear barbs (short = 5 kt, long = 10 kt) and isoshears for 40 kt, 50 kt, 60 kt from SPC mesoanalysis valid for 1900 UTC 31 March 2016.

2. BACKGROUND

2.1 Boundary layer

Storm mode and behavior is strongly modulated by the behavior of the PBL. One commonly accepted definition of the atmospheric boundary layer (ABL) is the “part of the troposphere that is directly influenced by the presence of the Earth’s surface, and responds to surface forcings with a timescale of about an hour or less” (Stull 1988). The terms ABL and PBL refer to the same thing and can be used interchangeably. For clarity, I will be using the term PBL. The CBL, sometimes referred to as the “mixed layer” because of the turbulent mixing that occurs within it, is a subtype of the PBL. Figure 2.1 conveys how these terms are interrelated.

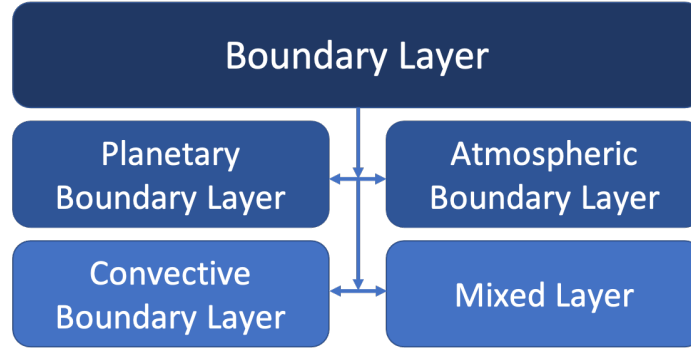


Figure 2.1. The relationships between terms used in boundary layer meteorology, as used in this thesis.

Since the PBL is closely tied to surface heating and cooling, it exhibits a diurnal variation (Fig. 2.2). Throughout the morning and afternoon, the boundary layer height begins to increase as buoyant thermal plumes rise, thereby eroding the capping inversion through turbulent mixing processes, hence the term “mixed layer” (Fig. 2.1) (Stull 1988). During this period, the boundary layer height can reach several kilometers (Stull 1988; Banghoff et al. 2018). In the evening hours, as the sun sets and convective turbulence dissipates, the boundary layer height begins to decrease, shrinking to only a few tens of meters (Stull 1988; Banghoff et al. 2018).

There are different sublayers within the daytime and nighttime boundary layers (Stull 1988) (Fig. 2.2). The main focus of this study is the CBL, which is composed of

(in order of height) the surface layer, mixed layer, and entrainment zone (Stull 1988; Angevine et al. 1994). The CBL is a mixed layer composed of buoyant, turbulent air that is driven by radiation and surface fluxes, in which air parcels buoyantly rise (Stull 1988). As such, the CBL is exclusive to the daytime heating hours (Fig. 2.2) and the growth of the CBL is dependent upon surface characteristics and the stability of the layer above the boundary layer, termed the free atmosphere (Cohn and Angevine 2000). It is important to monitor the CBL because it influences the potential for convection. The CBL is characterized by well-mixed temperature and moisture (i.e., profiles of these variables are relatively constant with height) (Fig. 2.3) (Stull 1988; Garratt 1992).

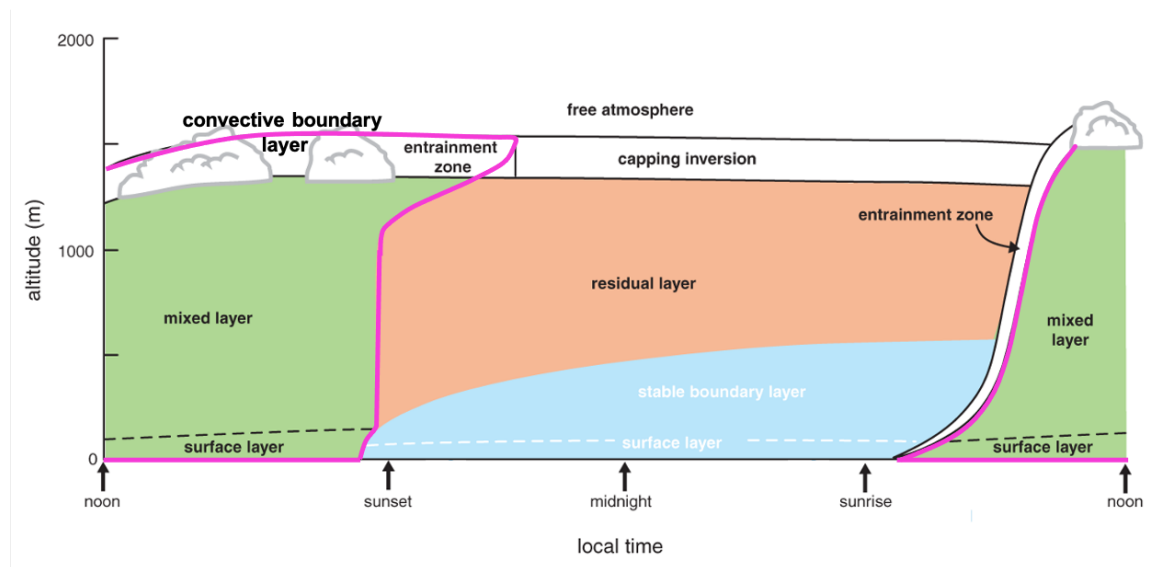


Figure 2.2. Conceptual diagram of the diurnal evolution of the PBL. The CBL is outlined in pink. (Adapted from Markowski and Richardson 2010.)

CBL depth is one parameter often used to characterize the CBL. The top of the boundary layer consists of unique characteristics that help make it identifiable. For example, the top of the boundary layer is marked by a temperature inversion (Stull 1988; Angevine et al. 1994). There are steep gradients in potential temperature and water vapor mixing ratio between the CBL and the free atmosphere (Stull 1988). The CBL height is often taken to be the middle of the entrainment zone, between

the top of the mixed layer and bottom of the free atmosphere (Stull 1988; Cohn and Angevine 2000). The depth of the CBL is pertinent for any boundary layer study or model (Angevine et al. 1994).

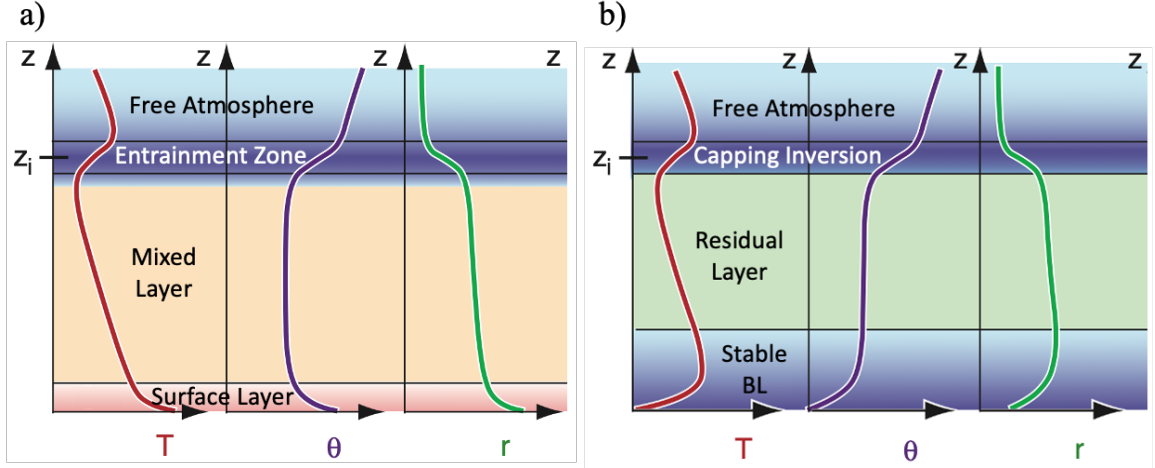


Figure 2.3. Idealized boundary layer profiles of (a) daytime and (b) nighttime temperature (T ; units K), potential temperature (θ ; units K) and mixing ratio (r ; units g m^{-3}). z_i is the boundary layer height, which is taken to be the halfway point between the top of the mixed layer (residual layer) and the entrainment zone (capping inversion) during the daytime (nighttime). (Adapted from Stull 2017.)

2.1.1 Role of the boundary layer in severe convective storms

Severe thunderstorms require a favorable juxtaposition of four ingredients: moisture, instability, lift, and shear (Johns and Doswell 1992; Markowski and Richardson 2010). Moisture increases instability, and instability is what allows air parcels to become positively buoyant and rise. Lift helps parcels reach the level of free convection (LFC), which is the point in the troposphere where parcels can continue to rise independently. Shear is a strong prognostic discriminator between nonsevere and severe storms. Severe thunderstorms are favored under strong speed and directional shear, which allows the thunderstorm to remain organized because it develops separate updraft and downdraft regions.

Boundary layer profiles are closely tied to moisture, instability, lift, and shear. Increases in moisture and instability create positively buoyant thermals, which mix the boundary layer and increase boundary layer depth. Shear also increases vertical mixing in the boundary layer, increasing boundary layer depth. When one or more of these ingredients is only marginally supportive of severe weather, small model errors can have a large impact on the forecast (Cohen et al. 2015). Environmental conditions influenced by the model’s PBL scheme can result in differences in the morphological characteristics (i.e., timing, location, mode, intensity) of the convection, which in turn impacts a forecaster’s assessment of the severe weather threat (Cohen et al. 2015, 2017). As such, there is a need to reduce errors in forecasting the vertical structure of the atmosphere, particularly the boundary layer, to better represent the convective environment (Cohen et al. 2017).

The severe storm environment in the SE-US has received comparatively little attention in regard to mesoscale modeling and PBL schemes (Cohen et al. 2015); however, in recent years more studies have begun to examine PBL modeling in the SE-US (e.g., Cohen et al. 2015; Cohen et al. 2017). Thermodynamic and kinematic properties of the PBL in this region are not only influenced by heat fluxes from diurnal heating, but also shear-driven eddies and large-scale vertical motion (Cohen et al. 2015). These processes need to be reflected in model simulations because the choice of PBL parameterization schemes can affect a model’s ability to accurately depict the SE-US severe storm environment (Cohen et al. 2015). PBL parameterization schemes are necessary because the vertical grids of most numerical weather prediction (NWP) models poorly resolve the PBL.

Cohen et al. (2015) and Cohen et al. (2017) found local PBL schemes (which consider immediately adjacent vertical levels) under-forecast PBL depth and do not fully mix the PBL in the SE-US, whereas non-local schemes (those that consider a deeper layer with multiple levels) overmix the PBL. Hybrid schemes represent environments that are not well mixed or strongly stable because vertical shear enhances mixing and limited instability inhibits mixing (Cohen et al. 2017). At night, most PBL schemes resulted in PBL depths that were too shallow (Cohen et al. 2017). All

PBL schemes examined in Cohen et al. (2017) also over forecasted MLCAPE in both daytime and overnight periods. They identified a need to improve a model’s ability to depict the PBL in the SE-US region, which would in turn improve the forecast and assessment of the severe weather threat. Accordingly, the differences between the Great Plains CBL and SE-US CBL need to be accurately characterized. This study will demonstrate the discrepancies between measured and numerically simulated PBL depth by means of comparison between vertically pointing radar observations and a high-resolution, nonhydrostatic NWP model. The case under consideration was a tornado that occurred just after sunset.

2.1.2 Bragg scattering

Thermals may overshoot the top of the boundary layer, entraining drier air from the free atmosphere into the CBL (Stull 1988). Such moisture gradients increase the refractive index of the atmosphere for electromagnetic waves (Wyngaard and LeMone 1980; Banghoff et al. 2018). Differences in indices of refraction satisfy a condition for Bragg scattering in the atmosphere (Rauber and Nesbitt 2018). Bragg scattering occurs when “electromagnetic waves impinge on regularly spaced objects or regions of air with different indices of refraction leading to constructive interference between the scattered waves” (e.g., Atlas 1959; Atlas 1960; Wolff 1998; Rauber and Nesbitt 2018). Constructive interference also occurs when scatterers are located at distances equal to half the radar wavelength (Wolff 1998; Rauber and Nesbitt 2018 and references therein).

Studies have demonstrated radars with 10 cm wavelengths (i.e. S-band) or longer are superior to shorter wavelength radars at detecting Bragg scattering (Ottersten 1969; Ralph 1995). Ralph (1995) performed a study to determine the threshold between Bragg scattering and Rayleigh scattering at various radar wavelengths. Based on this work, the range of values in which C- and X-band radars can detect Bragg scattering occur much less frequently than those at S-band (Ralph 1995).

2.1.3 Boundary layer profiling by S-band radars

Radars have been used to study the boundary layer using backscatter from inhomogeneities in the refractive index since at least the 1960s (e.g., Atlas et al. 1966; Hardy et al. 1966; Kropfli et al. 1968; Hardy and Katz 1969; Lane 1969, Tanamachi et al. 2019). They have the ability to detect wind, turbulence, and the stability of atmospheric layers (Gage and Balsley 1978). S-band (~ 10 cm) wavelength radars are commonly used for monitoring the CBL. They were designed to study boundary layer morphology and evolution, and to measure the refractive index structure with high spatial and temporal resolution (Chadwick et al. 1976; Waldinger et al. 2017). They are suitable for clear-air and precipitation studies because the S-band covers both Bragg scattering and Rayleigh scattering regimes (Battan 1959; Gossard 1990). The Rayleigh scattering regime dominates in most cases of precipitation where the scatterer is much smaller than the radar wavelength and the electric field is assumed to be constant across the scatterer (Rauber and Nesbitt 2018 and references therein). Scatterers detected in the examination of the boundary layer include hydrometeors, insects and birds, chaff, debris, and inhomogeneities in the refractive index (Gage and Balsley 1978; Gossard 1990). Using radar, there is the ability to determine the heights of the convective thermals in the boundary layer (Melnikov and Zrnić 2017), which aids in the detection of the boundary layer height. The use of these types of Doppler radars in field campaigns can aid in understanding the mesoscale structure of the atmosphere (Gage and Balsley 1978).

One type of S-band radar used to monitor the growth of the boundary layer is a frequency-modulated, continuous-wave radar. The phrase “continuous-wave” means the radar uses a high duty cycle, transmitting at or near 100% of the time (Fig. 2.4) (Richter 1969; Ince et al. 2003; Waldinger 2018). As a result, more energy is incident on scatterers than with a conventional pulsed radar, yielding high radar sensitivity (Richter 1969; Ince et al. 2003; Waldinger 2018). FMCW systems transmit a varying linear frequency-modulated waveform with a long pulse repetition period (Fig. 2.4) (Richter 1969; Ince et al. 2003; Waldinger et al. 2017). The received echoes are a

delayed version of the transmitted waveform, and when the two are combined, the resulting beat frequency is proportional to the range of the target (Richter 1969; Ince et al. 2003; Waldinger et al. 2017). The beat frequency signals are recorded and transformed into pulsed radar-like echoes using a Fourier transform (Eaton et al. 1995; Ince et al. 2003; Waldinger et al. 2017).

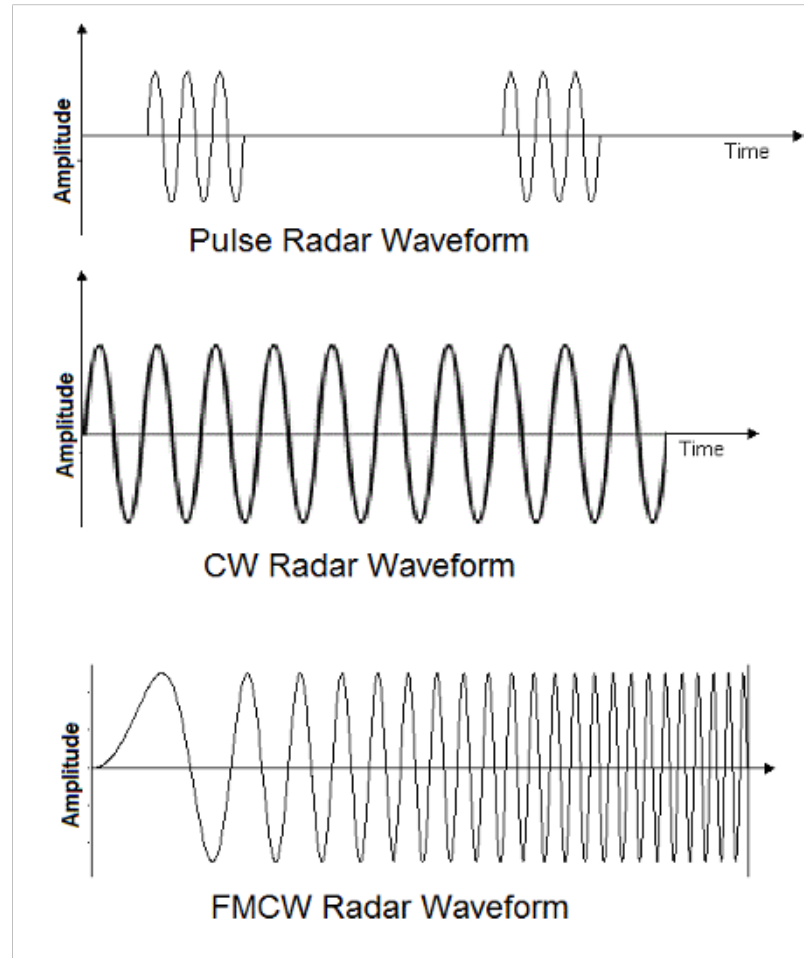


Figure 2.4. Waveforms for traditional pulsed radars (top), continuous-wave radars (middle), and frequency-modulated, continuous-wave radars (bottom). (From Hegazy et al. 2016.)

2.1.4 Interpreting FMCW data

Interpreting data from a vertically pointing, FMCW radar data is much different than interpreting data from a pulsed, volumetrically scanning radar. FMCW data

consist of vertical profiles of the conditions directly above the radar, whereas data from a volumetrically scanning radar are most often collected using a spiral step scanning pattern, scanning 360° and increasing elevation angle. If multiple layers with distinct characteristics are present, they may appear different on vertically pointing radar. Under quiescent, clear sky conditions, the layer exhibiting the highest reflectivity will likely be the top of the boundary layer, and any other layers with enhanced reflectivity are likely shear layers (Waldinger 2018). Similarly, Gossard (1990) states that internal layers within the boundary layer detected by radar are often locations of sharp temperature or humidity gradients. It is also common for insects or birds to produce brief high-reflectivity echoes (Waldinger 2018).

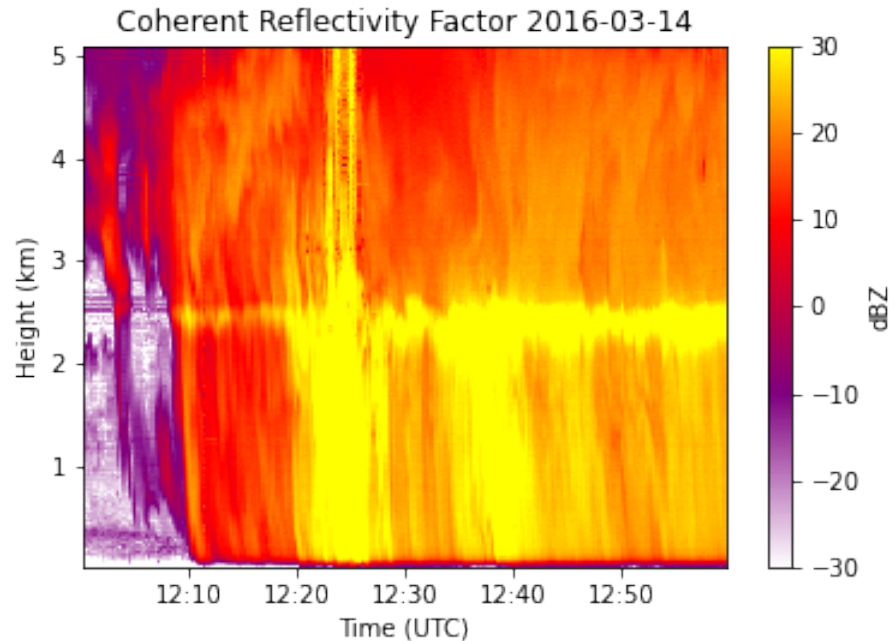


Figure 2.5. UMass FMCW coherent reflectivity factor (dBZ) from 1200 UTC to 1300 UTC 14 March 2016. The melting layer is located at ~ 2.5 km.

When precipitation is present in the column above the radar, the melting layer is identified as a local maximum in reflectivity aloft (Fig. 2.5) (Austin and Bemis 1950, Waldinger 2018). The reflectivity is greater in this region due to frozen particles becoming coated with liquid water as they begin to melt, increasing their index

of refraction, and having a larger cross-sectional area than the melted drops below (e.g., Austin and Bemis 1950; Rauber and Nesbitt 2018; Waldinger 2018). Above the melting layer, hydrometeors are frozen (i.e., snow flakes) and fall slowly, resulting in lower velocities (Doviak and Zrnić 1993, Fabry and Zawadzki 1995, Rauber and Nesbitt 2018). Below the melting layer, liquid drops fall much faster (Doviak and Zrnić 1993, Fabry and Zawadzki 1995). In the UMass FMCW data, the liquid precipitation sometimes has a velocity that exceeds the radar’s unambiguous velocity, resulting in incorrectly identified velocity values displaced by an integer multiple of the radar’s Nyquist interval. This phenomenon is known as velocity aliasing (Doviak and Zrnić 1993, Fabry and Zawadzki 1995, Rauber and Nesbitt 2018).

2.2 Issues with forecasting boundary layer height

The current U.S. upper air observational network is too sparse to capture boundary layer phenomena at length scales of 10 km or less (Wagner et al. 2019). Rawinsondes are a conventional observational tool for studying the boundary layer, but operationally, they are only launched twice daily at 0000 UTC and 1200 UTC in select locations in the U.S., resulting in coarse spatial (~ 100 km to 1000 km) and temporal resolution (Banghoff et al. 2018). Disadvantages of using radiosondes for field research include the high cost ($\sim \$500$) of each observation, the amount of labor that goes into each launch, and horizontal drift (Wagner et al. 2019). The existing WSR-88D network offers the potential for automated boundary layer height monitoring (e.g., Heinselman et al. 2009; Elmore et al. 2012; Bangoff et al. 2018) which increases the temporal resolution of boundary layer observations; however, the spatial resolution between WSR-88D sites is still on the order of 200 km to 300 km and WSR-88Ds cannot point vertically.

To supplement data from observations, PBL height can be calculated from NWP model output. Unfortunately, there can be large errors in boundary layer height estimates given by numerical models (e.g., Grimsdell and Angevine 1998; Stensrud and Weiss 2002; Cohen et al. 2017). Limited spatial and temporal resolution observations and inaccurate model predictions make it difficult to observe and forecast the height

of the boundary layer (Banghoff et al. 2018). Profiling instruments, such as FMCW radars, the National Oceanic and Atmospheric Administration (NOAA) Wind Profiler Network, the Collaborative Lower Atmospheric Mobile Profiling System (CLAMPS), and the Atmospheric Emitted Radiance Interferometer (AERI) can help alleviate some of these issues because they can capture the evolution of the boundary layer in near-real time (Wagner et al. 2019).

2.3 Data assimilation

NWP models use data assimilation (DA) to represent the initial state of the atmosphere as accurately as possible (Talagrand 1997). DA aims to combine observations and a prior model state to produce more accurate initial conditions for further integration of the model through the use of meteorological observations and physical laws, such as the conservation of mass and momentum (Talagrand 1997; Kalnay 2003). When observations are available, the background state predicted by the model is “updated” with the new observations (Talagrand 1997). The integration of the model is then restarted from this updated state and the process repeats (Talagrand 1997). There will inherently be uncertainty in both the observations and the model equations, so DA systems should not only provide a good representation of the atmospheric state, but also an estimate of the associated uncertainty (Talagrand 1997).

The goal of DA is to minimize the difference between observations and the updated model state, or analysis (Jung et al. 2008). Assimilation of observations into NWP models provides a statistically optimal combination of the model and observations for initialization (Xue et al. 2005). Over the past several decades, DA has improved the initial conditions of operational models, leading to improved NWP (Kalnay 2003). The assimilation of Doppler radar observations has shown to be particularly beneficial in the numerical prediction and analysis of severe convective storms (e.g., Xiao and Sun 2007; Snook et al. 2012; Tanamachi et al. 2013; Bachmann et al. 2020).

2.3.1 Ensemble Kalman filter

One technique used to capture uncertainty and model variability is ensemble forecasting. Ensemble forecasting generates multiple forecasts from the same model, each with slightly different initial conditions (Kalnay 2003). When a majority of ensemble members produce similar outcomes, there is greater confidence in the forecast. On the contrary, when there is greater spread amongst members, there is reduced confidence. Ensemble forecasting also provides information about forecast sensitivity and probabilistic forecast guidance (Snook et al. 2012). The forecast can be improved using ensemble averaging (Kalnay 2003).

One type of DA system commonly used for atmospheric data, and the one use in this study, is the ensemble Kalman filter (EnKF) (Evensen 1994, 2003; Houtekamer et al. 2005; Xue et al. 2005). EnKF uses an ensemble of forecasts to calculate a model spread (Snook et al. 2015). It predicts how all variables will change with one modification and updates all ensemble members. Given that the model and observations both have associated uncertainty, the ensemble spread after assimilation should be approximately equal to the uncertainty in the observations. Therefore, a key benefit to the EnKF method is that it helps capture uncertainty.

The EnKF technique can be used to assimilate both simulated and real data from various platforms, and it can be used on scales ranging from global models to mesoscale convective models (Houtekamer and Mitchell 1998; Snook et al. 2015). Because of its ability to handle complex, nonlinear, physical processes, EnKF is particularly suitable for convective scales (Jung et al. 2008). EnKF analyses characterize analysis uncertainty, which generates desirable initial conditions for ensemble forecasts (Snook et al. 2012). As the number of ensemble members increases, accuracy generally increases and the root-mean-square analysis error generally decreases (Houtekamer and Mitchell 1998).

The assimilation of Doppler radar observations through the EnKF technique has proven effective for initializing model states (Snook et al. 2012). Doppler velocity and radar reflectivity are the most commonly assimilated radar variables (Tanamachi

et al. 2013). When assimilating these two variables, EnKF methods have produced dynamically consistent wind, temperature, and microphysical fields for convective storms (Snook et al. 2012). Additionally, the more radars whose data are assimilated, the more realistic the model output tends to be (e.g., Tanamachi et al. 2013; Marquis et al. 2014; Supinie et al. 2016). In this study, conventional observations and radar reflectivity from the WSR-88D network surrounding the VORTEX-SE domain are assimilated into the Advanced Regional Prediction System (ARPS) model.

3. DATA AND METHODOLOGY

3.1 Data

High temporal resolution observations of CBL development have the potential to improve forecasts because the vertical structure of the atmosphere influences the timing, location, mode, and intensity of convection (Stull 1988; Markowski and Richardson 2010 and referenes therein). Quality control was performed on contaminated Doppler spectra from a vertically pointing, S-band, profiling radar deployed in northern Alabama during the VORTEX-SE field campaign. Once the spectra were cleaned, new moments were generated and radar derived boundary layer height observations were compared to forecast PBL height from the ARPS model as a verification metric of the new data set.

3.1.1 UMass FMCW observations

This study focuses on observations from the UMass FMCW collected during VORTEX-SE. The UMass FMCW (Fig. 3.1) was developed at the Microwave Remote Sensing Laboratory (MIRSL) (Eaton et al. 1995; Ince et al. 2000, 2003). It is an S-band, vertically pointing, single polarized, pulse compression radar. This radar is mounted on a truck for mobility, and is designed to be deployed at a fixed location continuously collecting observations for long periods of time (e.g., Tanamachi et al. 2019). The UMass FMCW uses a pair of 2.4-m diameter parabolic dish antennas, one for transmission and one for reception, each with 34 dB gain (Ince et al. 2003). The UMass FMCW has a high temporal (~ 16 s) and vertical (~ 5 m) resolution (Tanamachi et al. 2019).

The UMass FMCW was deployed to monitor the growth of the CBL over northern Alabama in both the 2016 and 2017 VORTEX-SE field experiments. In total, approximately 14 weeks of data were collected (55 days in 2016 and 53 days in 2017), ranging from clear air cases to severe thunderstorms (Tanamachi et al. 2019). In 2016, the UMass FMCW was deployed at the Tennessee Valley Research and Extension Center near Belle Mina, Alabama and operated almost continuously from 7

March to 30 April (Fig. 3.1). This site was selected because it is relatively free from clutter, and was collocated with other meteorological instruments.



Figure 3.1. The UMass FMCW at its 2016 VORTEX-SE deployment location near Belle Mina, AL. © Robin Tanamachi

The radar was configured to collect 256 frequency modulated sweeps over a 1.34-s interval to generate a Doppler spectrum. Twelve spectra were then averaged every 16.1 s. From these averaged spectra, the moments (reflectivity, Doppler velocity, and spectrum width) were calculated. Reflectivity (mm^6/m^3) is estimated from the signal to noise ratio (SNR) and calculated using:

$$\eta \approx 0.38 C_n^2 \lambda^{-1/3} \quad (3.1)$$

where η is reflectivity, C_n^2 is the refractive index structure parameter, and λ is radar wavelength. (3.1) assumes only Bragg scattering is present. Reflectivity (η) is different than reflectivity factor (dBZ), but in keeping with meteorological convention, reflectivity factor is referred to as just reflectivity. Each spectral profile in the 2016 data set comprised 1,024 spectra at 5-m height intervals from 0 to 5.1 km above radar level (ARL). In total, approximately 14,000 spectral profiles were collected over

the 2016 field campaign (Frasier and Waldinger 2016; Tanamachi et al. 2019). The UMass FMCW data are openly available through the Earth Observing Laboratory (EOL) archive (<https://data.eol.ucar.edu/dataset/527.016>).

3.1.2 Spurs

Unfortunately, the Doppler spectra collected in 2016 were contaminated by “spurs”, or spurious spectral peaks caused by high-voltage switching power supplies in the traveling wave tube amplifier, resulting in approximately 14,000 tainted spectral profiles. An example of such a contaminated spectral profile is shown in Fig. 3.2a. The spurs are evidenced as small, bright, horizontally elongated peaks. Electronic spurs can be distinguished from a naturally occurring peak in the spectra (e.g. a bird or bug) because they are time continuous and occur at nearly constant heights and amplitudes owing to their electronic origin, whereas echoes from birds and bugs vary widely in height and spectral power (Fig. 3.3). Spectral peaks at 0 m s^{-1} Doppler velocity are caused by ground clutter and antenna leakage (Waldinger 2018). Tanamachi et al. (2019) employed a median filtering technique (Fig. 3.2b) to eliminate most of the spurs, but the largest ones were still present, which degraded the quality of radar moments (e.g., reflectivity, Doppler velocity, and spectrum width) and hindered further analysis of these data (e.g., boundary layer height tracking). The traveling wave tube amplifier was replaced with a solid-state amplifier in 2017, which eliminated the spurs.

3.1.3 Description of in-painting algorithm

We aimed to rectify the unwanted spurs in the 2016 data in order to improve the quality of the moments. The method selected to remove and interpolate across the spurs was the Chan et al. (2016) “in-painting” method, which was developed to remove noise in 2D images. The version adapted for the UMass FMCW radar data can be found at <https://github.com/sbeverid/inpainting>.

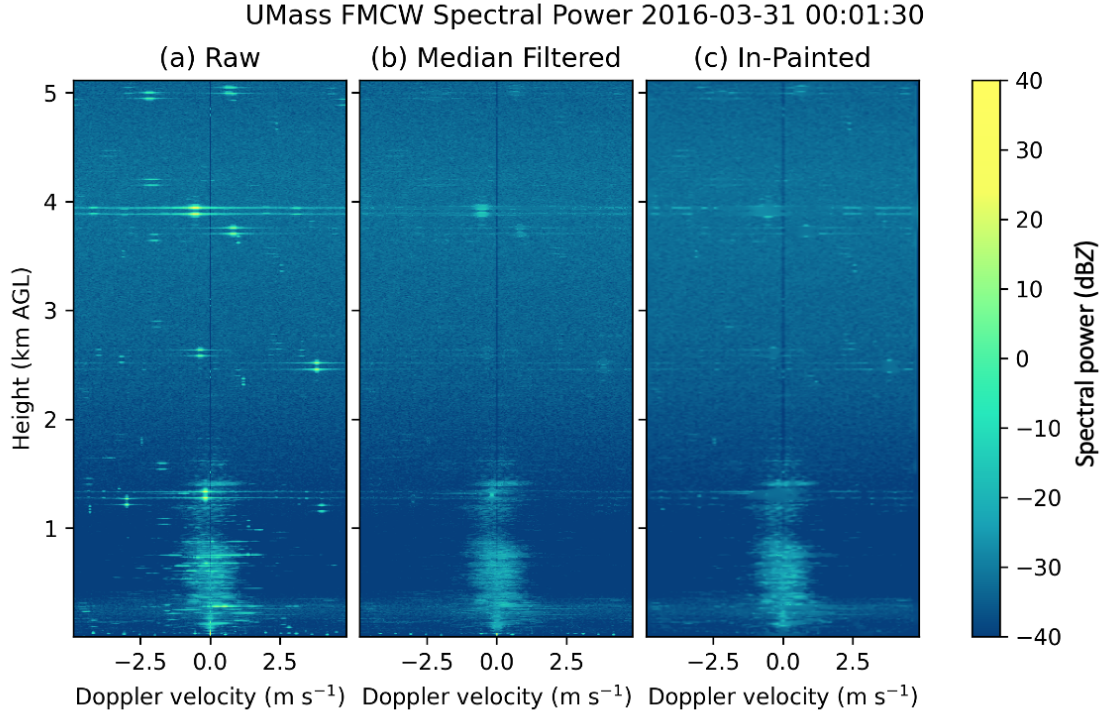


Figure 3.2. Spectral profile for a clear-air case on 31 March 2016: (a) raw spectral power (in dBZ); (b) as in a, but after application of the median filter; and (c) as in a, but after application of the in-painting method.

The main idea of the Chan et al. (2016) in-painting method is to take a corrupt image $\mathbf{y} \in R^n$ and use a maximum-a-posteriori estimation, with the goal of maximizing the posterior probability, to generate a denoised image (\mathbf{x}):

$$\begin{aligned}
 \hat{\mathbf{x}} &= \underset{\mathbf{x}}{\operatorname{argmax}} p(\mathbf{x} \mid \mathbf{y}) \\
 &= \underset{\mathbf{x}}{\operatorname{argmin}} -\log p(\mathbf{y} \mid \mathbf{x}) - \log p(\mathbf{x})
 \end{aligned} \tag{3.2}$$

where $p(\mathbf{y} \mid \mathbf{x})$ is some conditional probability, and $p(\mathbf{x})$ is a prior distribution of the image. We want to find an \mathbf{x} that maximizes the conditional probability and is the best approximation of the real image.

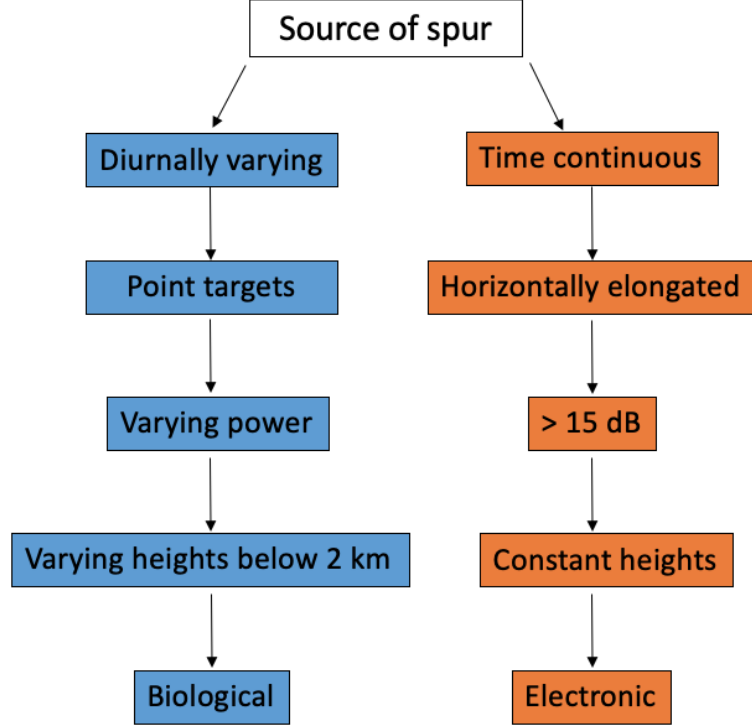


Figure 3.3. Flow chart of the logic for determining whether a peak in the Doppler spectra is biological or electronic in origin.

(3.2) can be written as an optimization problem:

$$\hat{\mathbf{x}} = \underset{\mathbf{x}}{\operatorname{argmin}} f(\mathbf{x}) + \lambda g(\mathbf{x}) \quad (3.3)$$

where $f(\mathbf{x}) \stackrel{\text{def}}{=} -\log p(\mathbf{y} \mid \mathbf{x})$ is the forward model of the image formation process, which tries to minimize the noise and other corruption happening from the image formation process, and $g(\mathbf{x}) \stackrel{\text{def}}{=} -(1/\lambda) \log p(\mathbf{x})$ is the regularization function that controls how natural the reconstructed image appears, and $\lambda > 0$ is the regularization parameter. λ controls how much prior information should be used to do the image reconstruction (i.e. how much $f(\mathbf{x})$ and $g(\mathbf{x})$ is needed). Using a λ that is too large can result in a loss of detail from the original image because too much weight will be

given to the prior. A very small λ can result in an image that still has a lot of corrupt pixels. $\log p(\mathbf{x})$ is the prior and $\log p(\mathbf{y} | \mathbf{x})$ is the probability mean square error.

It is difficult to solve the forward model and the prior at the same time, because we want a solution that will work for any prior. Therefore, a standard technique called alternating direction method of multipliers (ADMM) (Boyd et al. 2011; Chan et al. 2016) is used, where we introduce a new variable \mathbf{v} and add a constraint. The optimization problem is now:

$$(\hat{\mathbf{x}}, \hat{\mathbf{v}}) = \underset{\mathbf{x}, \mathbf{v}}{\operatorname{argmin}} f(\mathbf{x}) + \lambda g(\mathbf{v}), \quad \text{subject to} \quad \mathbf{x} = \mathbf{v} \quad (3.4)$$

One of the common ways to solve for a constrained optimization problem is to find the saddle point of the Lagrangian (Boyd et al. 2011). Since the Lagrangian itself is not usually stable, an augmented Lagrangian used here:

$$\mathcal{L}(\mathbf{x}, \mathbf{v}, \mathbf{u}) = f(\mathbf{x}) + \lambda g(\mathbf{v}) + \mathbf{u}^T(\mathbf{x} - \mathbf{v}) + \frac{\rho}{2} \|\mathbf{x} - \mathbf{v}\|^2 \quad (3.5)$$

This introduces a fourth term, which is added to prevent \mathbf{x} from moving too far away from \mathbf{v} , thus making making the Lagrangian more stable.

An approximate saddle point of (3.5) can be obtained by iteratively solving the following set of subproblems:

$$\mathbf{x}^{(k+1)} = \underset{\mathbf{x}}{\operatorname{argmin}} f(\mathbf{x}) + (\rho_k/2) \left\| \mathbf{x} - (\mathbf{v}^{(k)} - \mathbf{u}^{(k)}) \right\|^2 \quad (3.6)$$

$$\mathbf{v}^{(k+1)} = \mathcal{D}_{\sigma_k} \left(\mathbf{x}^{(k+1)} + \mathbf{u}^{(k)} \right) \quad (3.7)$$

$$\mathbf{u}^{(k+1)} = \mathbf{u}^{(k)} + \left(\mathbf{x}^{(k+1)} - \mathbf{v}^{(k+1)} \right) \quad (3.8)$$

$$\rho_{k+1} = \gamma_k \rho_k \quad (3.9)$$

(3.6), (3.7), (3.8) are scaled multipliers where \mathcal{D}_{σ_k} is an image denoiser algorithm and $\sigma_k \stackrel{\text{def}}{=} \sqrt{\lambda/\rho_k}$ is the “noise level” that the denoiser takes and controls the strength of the denoiser. A larger σ_k results in a smoother image, whereas a smaller σ_k retains more details from the original image. (3.6) is an inversion step and (3.7) is a denoiser

step, involving the prior. These equations are repeatedly solved until the algorithm converges.

For the Chan et al. (2016) in-painting method, the problem takes the following form:

$$\hat{\mathbf{x}} = \underset{\mathbf{x}}{\operatorname{argmin}} \frac{1}{2} \|\mathbf{S}\mathbf{x} - \mathbf{y}\|^2 + \lambda g(\mathbf{x}) \quad (3.10)$$

where \mathbf{S} is a diagonal matrix which contains a list of pixels and \mathbf{x} is a 1D array (Fig. 3.4a). Therefore, once you apply the matrix \mathbf{S} to the original, corrupt image, you will get an image with the corresponding missing pixels. Implementation of \mathbf{S} is done using a mask (Fig. 3.4b).

(a) input					(b) mask					(c) output				
0	0	0	0	0	1	1	1	1	1	0	0	0	0	0
0	0.5	0.5	0.5	0	1	1	1	1	1	0	0.5	0.5	0.5	0
0	0.5	1	0.5	0	1	1	0	1	1	0	0.5	0.5	0.5	0
0	0.5	0.5	0.5	0	1	1	1	1	1	0	0.5	0.5	0.5	0
0	0	0	0	0	1	1	1	1	1	0	0	0	0	0

Figure 3.4. Simplified example of the in-painting process using a 5×5 matrix with (a) a peak in the center pixel; (b) implementation of a mask around the peak; and (c) the output image with the peak filled in according to surrounding data.

The inversion step for in-painting becomes:

$$\hat{\mathbf{x}} = \underset{\mathbf{x}}{\operatorname{argmin}} \frac{1}{2} \|\mathbf{S}\mathbf{x} - \mathbf{y}\|^2 + \frac{\rho}{2} \|\mathbf{x} - \tilde{\mathbf{x}}\|^2 \quad (3.11)$$

and the solution becomes:

$$\hat{\mathbf{x}} = (\mathbf{S}^T \mathbf{S} + \rho \mathbf{I})^{-1} (\mathbf{S}^T \mathbf{y} + \rho \tilde{\mathbf{x}}) \quad (3.12)$$

(Fig. 3.4c). $\mathbf{S}^T \mathbf{S}$ is a diagonal matrix with binary entries: pixel present = 1 or pixel not present = 0. The closed form solution can be executed using element-wise division, or in this case, “pixel-wise” division for all pixels.

In essence, each UMass FMCW spectral profile (e.g., Fig. 3.2a, Fig. 3.5a) was treated as a $256 \times 1,024$ pixel image. The Chan et al. (2016) in-painting code requires a first guess for the locations of noise spikes in an image, which were provided by labeling local extrema in the Laplacian of the spectral profile. After these extrema were masked, the dynamic range of the UMass FMCW spectral power (ranging from -50.5 dBZ to +47.6 dBZ) was scaled down to the normalized range (0, 1), as required by the Chan et al. (2016) in-painting code (Fig. 3.5b). The Chan et al. (2016) in-painting code then filled in the masked area according to surrounding data. In cases in which the holes created by the masking procedure were too large for the in-painting method to fill, the masked $256 \times 1,024$ spectral profile was down-sampled to a 128×512 -pixel image, to which the in-painting code was then applied. The resulting spectral profile was then scaled back up to the original size and dynamic range. Lastly, regardless of whether the down-scaling substep occurred or not, those portions of the spectral profiles that were not masked in the Laplacian filtering step were restored. The resulting spectral profiles are hereafter referred to as the “in-painted” spectral profiles (e.g., Fig. 3.2c, Fig. 3.5c).

The Chan et al. (2016) in-painting method is superior to simplistic methods, such as linear interpolation, because the denoiser is more powerful. Denoisers have an image prior, either implicitly or explicitly defined, that ensures the reconstructed image is close to the distribution of images, whereas simple linear interpolation does not. A limitation regarding the Chan et al. (2016) in-painting method is that completely saturated pixels, such as in instances where aircraft pass over the radar, cannot be fixed by the in-painting method because the noise floor is raised. In the 2016 data set, this was not a common issue and cases were easily eliminated by inspection.

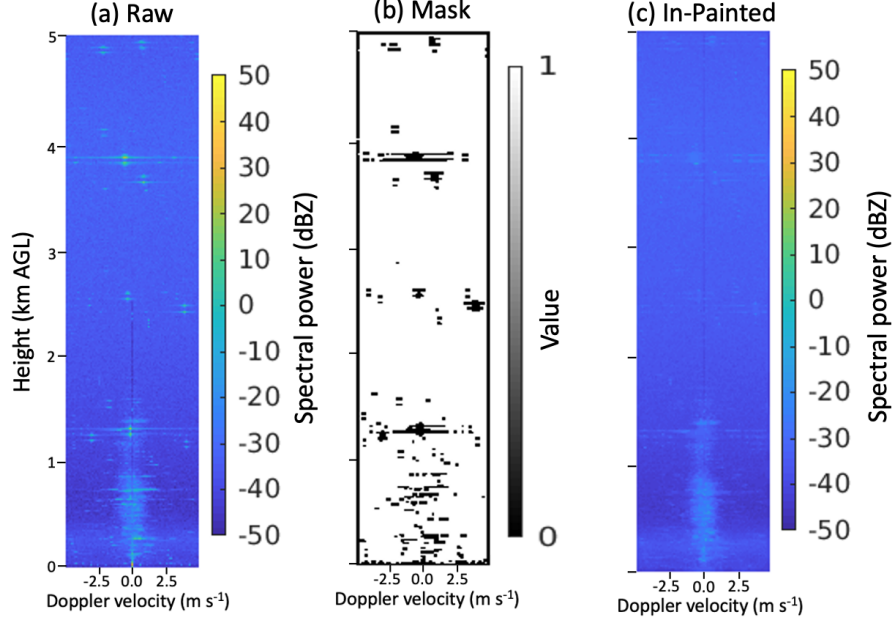


Figure 3.5. Example of the in-painting process for a Doppler spectral profile at 0000 UTC 31 March 2016 with (a) the raw spectral profile containing the peaks; (b) implementation of a mask around the peaks with the normalized dynamic range; and (c) the output in-painted image with the peaks filled in according to surrounding data.

3.1.4 Spectral power differences

To evaluate the performance of the Chan et al. (2016) in-painting method relative to the median filter, spectral power differences were calculated and plotted. Multiple three-panel plots were produced containing spectral power differences for time indices 0, 100, and 200, coinciding with approximately the beginning, middle, and end of a given hour. These time indices were sufficient to give an overview of how well the in-painting method performed compared to the median filter. To visualize the spectral power differences, histograms were produced of spectral profile pixels for each 5-dB spectral power difference bin. The bins (-5 dB, 0 dB) and (0 dB, 5 dB) were masked, because their frequencies dominated the histograms by several orders of magnitude.

3.1.5 Regenerating UMass FMCW moments

The moments of Doppler spectra are the basis of three primary weather radar variables: reflectivity, Doppler velocity, and spectrum width. When the quality of the Doppler spectra are compromised, it impacts the quality of these derived spectral moments. Once the quality of the Doppler spectra were improved, we generated a new version of UMass FMCW spectral moments from the in-painted spectra.

The velocities of targets within a radar sample volume vary due to wind shear, variations in target fall speeds, small-scale turbulent motions (Rauber and Nesbitt 2018 and references therein), and other factors (Doviak and Zrnić 1993). The radial velocity assigned to that sample volume is a representation of the power weighted average target motion over all targets within the sample volume (Rauber and Nesbitt 2018 and references therein). When the different phase shifts for all of the different pulse-pairs taken within a given sample volume are aggregated, a spectrum of velocities is produced (Rauber and Nesbitt 2018 and references therein).

Traditionally, radar reflectivity is calculated using noise-subtracted power measurements (Ulaby et al. 1982, Doviak and Zrnić 1993, Pazmany and Haimov 2018). In the UMass FMCW data, the noise floor was assumed to be a constant function of range, but in reality, there are subtle changes in the noise floor. For example, temperature fluctuations change receiver gain, which results in changes in the noise floor. Unwanted striping was present in the reflectivity and signal to noise ratio (SNR) fields, even after the application of the Chan et al. (2016) in-painting, because the largest spurs were accompanied by large jumps in the noise floor. To mitigate the unwanted striping in reflectivity and SNR, we applied the coherent power (CP) technique (Pazmany and Haimov 2018). The CP technique uses coherent reflectivity factor, which is the reflectivity derived from the coherent signal to noise ratio (SNC). SNC is the signal to noise ratio derived from the coherent power, which does not require noise subtraction. Instead, it assumes each signal has a different noise sample and when averaging the noise samples, the noise gets smaller and smaller because of the random phase. Therefore, a benefit to using coherent reflectivity is that it is

derived directly from the pulse pair correlation and does not require estimating and subtracting noise (Pazmany and Haimov 2018). This also results in an inherently unbiased signal.

3.1.6 Boundary layer height detection algorithm

Since one of the objectives of VORTEX-SE was to quantitatively assess boundary layer growth, an objective method to measure the boundary layer height in reflectivity observations was needed. Deriving boundary layer height from the UMass FMCW radar served two purposes: 1) a metric to evaluate the improvement of the in-painted Doppler spectra on downstream products, and 2) a comparison to the ARPS modeled PBL depth at Belle Mina, Alabama.

The method selected to estimate the CBL depth was the boundary layer height detection algorithm of Lange et al. (2015). This algorithm employs an extended Kalman filter (EKF) which combines past and present CBL height estimates with an *a priori* estimate and an analytical model of the CBL-to-free atmosphere transition reflectivity profile to provide time-continuous CBL height estimations (Lange et al. 2015). The reader is directed to Lange et al. (2015) for additional information regarding the boundary layer height detection algorithm beyond what is discussed below.

The first step in the boundary layer height detection algorithm is a preprocessing step to generate a “clean” time-height reflectivity profile where Bragg scattering dominates (Lange et al. 2015). A median filter is used to remove noise caused by Rayleigh scatterers, such as bioscatterers, and instrumentation effects (Lange et al. 2015). The resulting reflectivity image is an approximation of what the radar would see if only Bragg scattering was present, from which the CBL depth can then be estimated (Lange et al. 2015). The next step is to run the EKF (Lange et al. 2015). The EKF requires initial guesses for the *a priori* state vector (i.e., the previous time step’s reflectivity profile), *a priori* state vector error covariance matrix factor, atmospheric state-noise covariance matrix factor, and the bounds of the filter (Lange et al. 2015). Lastly, the measurement noise covariance matrix is computed under the assumption

of ergodicity (Lange et al. 2015). With each iteration of the EKF, a new, *a posteriori* estimate of the CBL height is generated.

One limitation to the boundary layer height detection algorithm is that the Kalman filter assumes relatively slowly varying quantities. Additionally, the algorithm is limited by error covariances, so there are no large jumps in boundary layer height. Tracking the stable boundary layer and elevated residual layer was beyond the scope of this study because the focus of VORTEX-SE was on the CBL.

To quantify the improvement of the algorithm with the in-painted moments, histograms were produced of the frequency of PBL height values. These are discussed in the next chapter.

3.2 Numerical model

As part of other VORTEX-SE-related research at Purdue, we performed a high-resolution numerical simulation of the northern Alabama domain for one IOP from the 2016 campaign. From this, we generated an ensemble of boundary layer states against which the UMass FMCW-derived boundary layer heights could be compared. Numerical simulations were performed using the ARPS model. The ARPS model was developed at the Center for Analysis and Prediction of Storms at the University of Oklahoma (Johnson et al. 1994; Xue et al. 2000). It is a fully 3D, compressible, and nonhydrostatic model designed for mesoscale to convective scale studies (Johnson et al. 1994; Xue et al. 2000). The governing equations are transformed from Cartesian coordinates to curvilinear coordinates to allow for stretched grids and terrain (Johnson et al. 1994). Additionally, ARPS has the ability to change grid shape with time, which allows for higher resolution grids in regions with larger gradients (Johnson et al. 1994).

ARPS employs a non-local boundary layer parameterization scheme. It contains different input options that determine how PBL depth is calculated. For the method selected in this study, the initial PBL depth (h_0) is scaled by the frictional velocity (u_*):

$$h_0 = u_*/f \tag{3.13}$$

where f is the Coriolis parameter. Then, PBL depth either decreases or increases depending on whether the boundary layer is stable or unstable. Stability is determined based on the bulk Richardson number:

$$Ri_b = \frac{g}{\theta_0} \frac{(\theta_h - \theta_s) h}{U_h^2} \quad (3.14)$$

where g is gravitational acceleration, U_h and θ_h are the wind speed and potential temperature at the top of the PBL, and θ_0 and θ_s are the reference and surface potential temperatures, respectively. If $Ri_b > 0$, it is assumed there is a stable boundary layer and the depth is calculated as follows:

$$\frac{dh}{dt} = T^{-1} (h_e - h) \quad (3.15)$$

where

$$T = -\frac{3}{4} \frac{(\theta_h - \theta_s)}{\partial \theta_s / \partial t} \quad (3.16)$$

and

$$h_e = 0.15 \theta_0 \frac{f U_h^2 \sin \alpha \cos \alpha}{g |\partial \theta_s / \partial t|} \quad (3.17)$$

where h_e is the equilibrium height and α is the angle between the wind at the top of the PBL and the surface wind:

$$\alpha = \tan^{-1} (u_h / v_h) - \tan^{-1} (u_s / v_s) \quad (3.18)$$

On the contrary, if $Ri_b < 0$, the boundary layer is assumed to be unstable and depth is calculated with:

$$\left(\frac{h^2}{(1 + 2A)h - 2B\kappa L} \right) \frac{dh}{dt} = \frac{(\overline{w'\theta'})_s}{(\partial \theta / \partial z)_h} \quad (3.19)$$

where $A = 0.2$, $B = 2.5$, κ is the von Karman constant, $(\overline{w'\theta'})_s$ is the vertical heat flux at the surface, L is the Obukhov length defined by:

$$L = -\frac{u_*^3 \theta}{\kappa g (\overline{w'\theta'})_s} \quad (3.20)$$

Regardless of the method selected to calculate PBL depth in the ARPS model, PBL depth is a diagnostic quantity. Because ARPS PBL depth is diagnostic, it is not tied to turbulence.

Benefits to using the ARPS model include: it has self-contained data ingest, quality control and objective analysis packages, a DA system which includes single-Doppler velocity and thermodynamic retrieval algorithms, a forward prediction component, and a self-contained post-processing, diagnostic and verification package (Xue et al. 2000). The model is essentially run via two main steps: initialization and iteration (Johnson et al. 1994). The initialization step generates an initial model state and the iteration step integrates the model equations at each grid point, through successive time steps (Johnson et al. 1994). The initialization period is shorter than the iteration period (Johnson et al. 1994).

To examine the 31 March 2016 tornadic VORTEX-SE case, we performed numerical simulations of the weather conditions on three one-way nested grids at horizontal grid spacings of $\Delta x = 6$ km, 3 km, and 1 km (Fig. 3.6). All grids had 53 vertical levels stretching from ~ 20 m near the surface to 773 m aloft. For these experiments, we used an ensemble of 40 members.

3.2.1 Model data

Five-minute observations from the Automated Surface Observing System (ASOS) (<https://www.ncdc.noaa.gov/data-access/land-based-station-data/land-based-datasets/automated-surface-observing-system-asos>) were assimilated into ARPS for all experiments. These surface observations consisted of temperature (T), dew point temperature (T_d), pressure (p), and the zonal (u) and meridional (v) components of the wind.

In addition to surface observations, Level II WSR-88D radar data were also assimilated. These data were downloaded from the National Centers for Environmental Information NEXRAD data archive (<https://www.ncdc.noaa.gov/nexradinv/>). Radar reflectivity and radial velocity data were assimilated into the model using the EnKF method. Only WSR-88D data from 1800 UTC 31 March 2016 to 0300 UTC 1

April 2016 were assimilated because the focus of this study is on the tornadic round of evening convection.

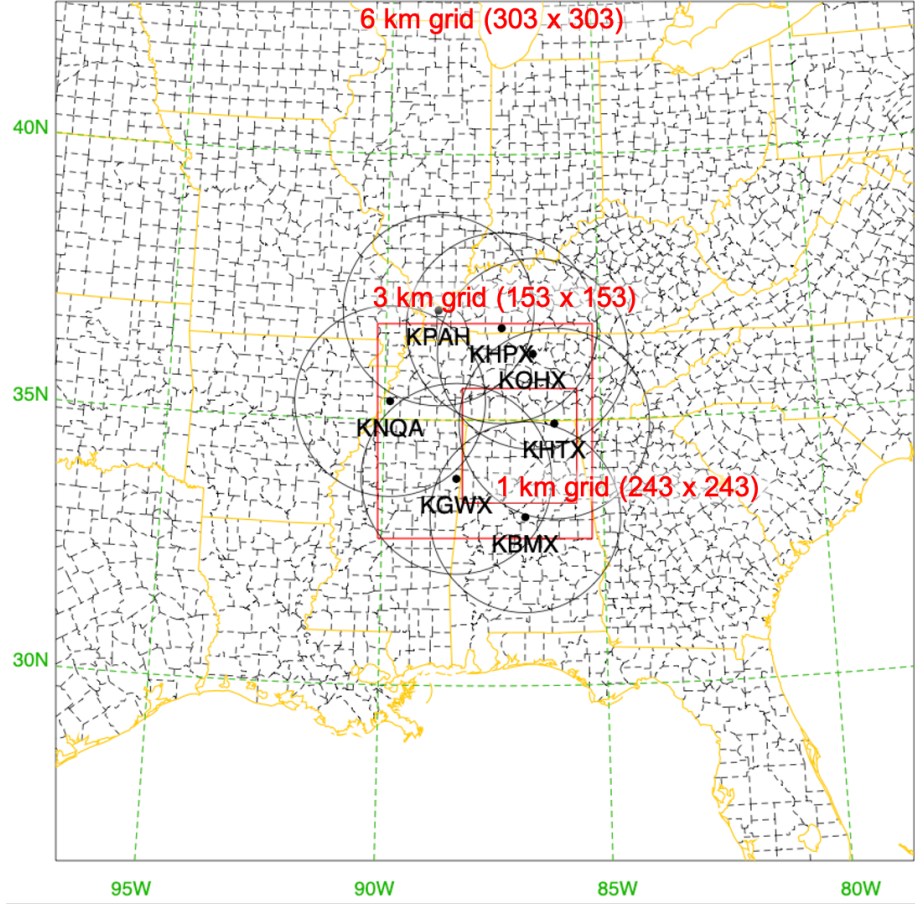


Figure 3.6. 6 km (outermost box), 3 km, and 1 km (innermost, red box) grid domains, including the locations of the WSR-88D radars that were assimilated.

A total of three test experiments were performed (Table 3.1). These experiments are further detailed below.

3.2.2 6 km simulation

The 6 km simulation had a grid size of $303 \times 303 \times 53$ and covered the VORTEX-SE domain (Fig. 3.6). Data from the North American Mesoscale Forecast System (NAM), an operational NWP model which has a horizontal grid spacing of 40 km, was used for the initial conditions and boundary conditions. NAM output can be

accessed at <https://www.ncdc.noaa.gov/data-access/model-data/model-datasets/north-american-mesoscale-forecast-system-nam>. A 6-hour spin up period (1200 UTC to 1800 UTC 31 March 2016), in which no data were assimilated, was used to allow the model to become steady (Fig. 3.7). ASOS observations were assimilated from 1800 UTC 31 March 2016 to 0300 UTC 1 April 2016. Output for the 6 km simulation was generated every 15 minutes (Fig. 3.7).

Table 3.1. A brief description of the experiments, including the grid sizes and data assimilated.

Experiment Type	Horizontal Grid Spacing	Description
Background	6 km	Assimilated surface obs., served as the background for the 3 km experiment
sfc+88D	3 km	Assimilated surface obs. and WSR-88D data, served as the background for the 1 km experiment
sfc+88D	1 km	Assimilated surface obs. and WSR-88D data

3.2.3 3 km simulation

The 3 km simulation had a grid size of $153 \times 153 \times 53$ and covered northern Alabama (Fig. 3.6). The aforementioned 6 km simulation served as the initial conditions and boundary conditions for the 3 km simulation. This simulation assimilated surface and radar observations from KBMX, KGWX, KHPX, KHTX, KNQA, KOHX, and KPAH every 5 minutes. Output for the 3 km simulation was generated every 5 minutes (Fig. 3.7).

3.2.4 1 km simulation

The 1 km grid was $243 \text{ km} \times 243 \text{ km}$ in size and was centered over Priceville, Alabama (Fig. 3.6) where the tornado occurred at 0154 UTC. The 1 km simulation was initialized using initial and boundary conditions generated from the 3 km simulation. To prevent the model from becoming unstable, surface and radar observations were assimilated at every other grid point. Output for the 1 km simulation was generated every 5 minutes (Fig. 3.7).

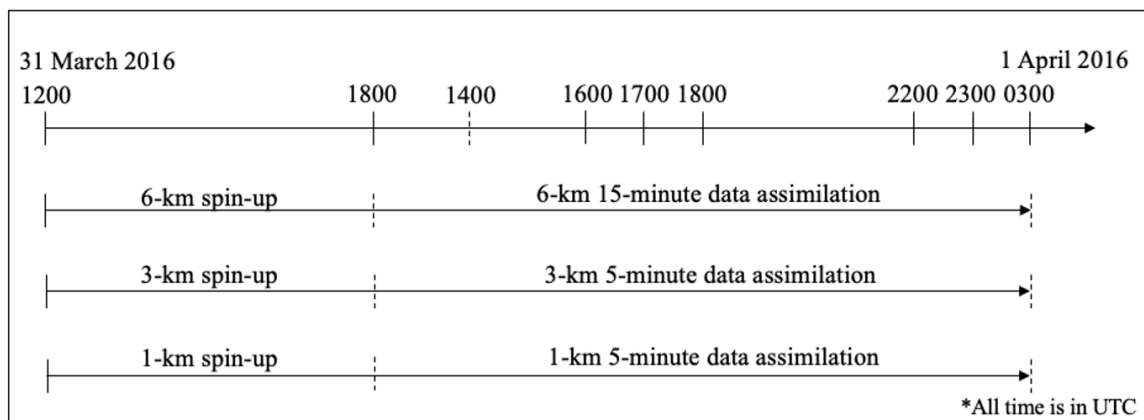


Figure 3.7. A timeline of the 6 km, 3 km, and 1 km experiments. All times are in UTC.

Thermodynamic profiles (i.e., a model sounding) were extracted from the 1 km simulation at the grid point closest to Belle Mina, Alabama, where the UMass FMCW radar was deployed. This allowed for a straightforward comparison of the model-derived boundary layer height with the radar-derived boundary layer height. The comparison was done via a time series analysis.

4. RESULTS

4.1 Spectral power differences

When examining the spectral power difference plots (e.g., Fig. 4.1f), areas that are brighter and have higher spectral power difference values indicate an improvement in the removal of the spurs (i.e., the spurs were more effectively flattened by the Chan et al. (2016) in-painting method than the median filter method). Regions that are darker with negative spectral power indicate spurs that were more effectively removed by the median filter than the Chan et al. (2016) in-painting method. Additionally, for the in-painting method to perform better than the median filter method, we expect a right-tailed distribution in the spectral power difference histograms (e.g., Fig. 4.2).

4.1.1 Clear air

For clear air (i.e., non-precipitation containing) spectra, the median filter method did a good job at removing the spurs, particularly the smaller peaks, as can be seen from the raw minus median filtered panels of the spectral power difference plots (Fig. 4.1d). However, the Chan et al. (2016) in-painting method better removed the larger peaks (Fig. 4.1e), as indicated by the greater spectral power differences there. There were negative spectral power difference values when the in-painted spectra were subtracted from the median filtered spectra, indicating the Chan et al. (2016) in-painting method did not remove the small peaks as well as the median filter method (Fig. 4.1f).

The spectral power difference histograms for clear air cases have right-tailed distributions (Fig. 4.2). The raw minus median filtered spectral power difference histograms (Fig. 4.2a) have a greater number of spectral profile pixels in the bins with lower spectral difference (i.e., $\sim < 20$ dB) compared to the raw minus in-painted histograms (Fig. 4.2b), whereas the raw minus in-painted histograms have a greater number of spectral profile pixels in the bins > 35 dB (Fig. 4.2e). This can be seen in Fig. 4.2d-f, which zoom in on the higher spectral power differences to show the detail in the improvement in the number of spectral profile bins between the raw minus

median filtered and raw minus in-painted. Given the negative spectral power difference values, the Chan et al. (2016) in-painting method retains some artifacts from small peaks. This affirms the Chan et al. (2016) in-painting method better removes the large spurs. While the median filter may smooth out small-amplitude spurs, it also wipes out spectral features with small amplitudes that we wish to retain. Examples include monodisperse precipitation spectral peaks as might be encountered in the presence of size sorting, or bioscatterer activity, whereas the in-painting method retains these features owing to its data restoration step in unmasked regions.

4.1.2 Precipitation

In spectral profiles containing precipitation, there are fewer spurs present, because power associated with the spurs does not exceed that from the rain in most cases (Fig. 4.3). Again, the Chan et al. (2016) in-painting method better removes the large spurs, particularly in regions of the spectra unaffected by rain. This is evidenced by the greater spectral power difference and higher dB values in those regions in the raw minus in-painted (Fig. 4.3e) and median filtered minus in-painted (Fig. 4.3f) panels. Again, small peaks are not as well removed with the Chan et al. (2016) in-painting method because they evade masking during the initial Lagrangian peak-finding step.

The spectral difference histograms for precipitation cases also have right-tailed distributions (Fig. 4.4). However, when compared to the corresponding histograms for clear-air cases, the frequencies in each bin are smaller. This is because, in many instances, the spurs have lower power than, and are therefore obscured by, the rain signal. Negative spectral differences come mostly from differences along the zero isodop and the edges of the peaks (Fig. 4.4b-c). This provides further evidence the Chan et al. (2016) in-painting performs well on large peaks, but does not handle smaller peaks as well.

4.2 Moments

The moments generated from the median filtered Doppler spectra have spurious reflectivity and SNR peaks at constant altitudes caused by the largest spurs (bold horizontal lines at approximately 1.3 km, 2.6 km, and 3.9 km in Fig. 4.5a-d). The Chan et al. (2016) in-painting method removed some of the unwanted horizontal striping, resulting in cleaner derived moments (Figs. 4.5e-h and 4.6e-h). The use of coherent reflectivity and SNC, which are not noise floor-dependent, helped reduce the effect of receiver saturation that we dubbed, “horizon glow” (Fig. 4.5e-h). This is also evident when comparing reflectivity (Fig. 4.7) and coherent reflectivity (Fig. 4.8) fields for the entire 2016 VORTEX-SE campaign.

4.3 Boundary layer height detection

Tanamachi et al. (2019) noted that an automated boundary layer height detection algorithm (Lange et al. 2015), which operated purely on the reflectivity, struggled to identify the top of the boundary layer in the presence of the spurious reflectivity peaks caused by the spurs in the Doppler spectra, even after median filtering was applied. It can be seen in the example shown in Fig. 4.9a that the algorithm misidentified the spurious reflectivity peaks as the top of the CBL. The combined application of the Chan et al. (2016) in-painting and CP technique methods reduced the amplitudes of these peaks, leaving the Bragg scatter at the top of the CBL as the dominant signal in clear air.

Qualitatively (e.g., Fig. 4.9b) and quantitatively (e.g., Fig. 4.10b), the automated boundary layer height detection algorithm performs much better on this new reflectivity field. For the quantitative assessment, histograms were generated for a subsample of 24 hours of clear air boundary layer height detection observations using both median filtered and in-painted moments. The median filter method identifies more PBL heights at 1.3 km associated with a maximum in reflectivity caused by the spurs (Fig. 4.10a). The in-painting method better removes the spurs, which reduces the number of misidentified PBL heights (Fig. 4.10b). There is another local peak in

the median filtered histogram in the bin centered around 400 m ARL, which is the top of the horizon glow layer. With the horizon glow removed by the CP technique, there are now detections of PBL depth in the bottom two bins that used to be obscured by the horizon glow.

There were instances where the boundary layer height detection algorithm failed to accurately detect the decaying CBL, and instead began tracking the residual layer. It may be possible to tag boundary layer retrievals in the algorithm with a quality flag based on factors such as time of day, net radiative flux sign, presence of clouds and precipitation, etc. However, a data quality flag is beyond scope of this study.

4.4 ARPS model comparison

As a demonstration of the potential diagnostic value of the PBL depth values derived from these improved moments, they were compared with PBL depth estimates from a state-of-the-art NWP model, the ARPS (Xue et al. 2000). At early times (1800 UTC to 2100 UTC) in the ARPS simulations, calculated PBL depths followed the UMass FMCW observations of boundary layer depth (Fig. 4.11). There was particularly good agreement between the PBL depths derived from UMass FMCW and the ensemble mean PBL depth from the ARPS model between 1930 UTC and 2030 UTC. Given this was a multi-hour, pre-convective environment (1800 UTC to 2200 UTC), which is often a difficult period to model, the ARPS and UMass FMCW PBL heights compared quite well. However, after 2200 UTC, the PBL depth derived from the UMass FMCW observations continued increasing, while the PBL depth in nearly all the ARPS ensemble members decreased to 0 m by 2300 UTC, about an hour before local sunset (0008 UTC) and two hours before the onset of precipitation. The divergent trend can partially be explained by the boundary layer height detection algorithm applied to the UMass FMCW observations failing to accurately track the decaying CBL. We expect the CBL to begin decaying when net radiative flux at the surface changes sign (from downward to upward). Instead, it began tracking the residual layer (Fig. 4.12). If the algorithm were to track the decaying CBL seen in

the UMass FMCW observations, the PBL depths would align more closely with the modeled PBL depths from ARPS.

We sought to further explain the divergent trends in PBL depth between the UMass FMCW and the ARPS model at and after 2300 UTC by examining the ARPS model output for temperature, pressure, and humidity, which were used to create model soundings. Local sunset was not until 0008 UTC, so the cessation of turbulent mixing does not explain the collapse of PBL depth in the ARPS model an hour beforehand. Additionally, there were no simulated storms nearby generating near-surface cold pools that would stabilize the boundary layer at Belle Mina; the simulated surface potential temperature at Belle Mina stayed nearly constant throughout this period (Fig. 4.13). Therefore, a change within the mixed layer between 2200 UTC and 2330 UTC must be responsible for the reduction in simulated PBL depth.

Model soundings were produced for 2200 UTC (before ARPS PBL depth started to decrease) and 2330 UTC (after ARPS PBL depth started to decrease) at the grid point closest to Belle Mina, Alabama, where UMass FMCW was located. In a skew-T from an example ensemble member (member 1), it can be seen that the layer between 900 hPa and 800 hPa warmed and dried between 2200 UTC and 2330 UTC, while the surface conditions remained relatively constant (Fig. 4.14). This warming of the upper boundary layer decreased the lapse rate and stabilized the boundary layer, leading to a reduction in the calculated PBL depth.

Cohen et al. (2015, 2017) document similar inconsistencies between observed and modeled boundary layer depths over the SE-US in operational models. However, they found that local PBL parameterization schemes tended to overmix and stabilize the boundary layer more than nonlocal PBL schemes. Since ARPS has a nonlocal PBL parameterization scheme, we do not believe that this is the primary source of the simulated PBL stabilization. We speculated subsidence could be occurring in the ARPS model, causing compressional warming. We investigated this by plotting ARPS ensemble mean vertical velocity (w) in the 900 mb to 800 mb layer where the warming was occurring (Fig. 4.15). There is a period of subsidence from ~ 2220 UTC to 2250 UTC that could be responsible for the warming. Additionally, there

were horizontal convective rolls occurring throughout the domain during this period (not shown), which is why w in Fig. 4.15 switches between positive and negative. Other plausible causes of the warming and drying could be latent heat release by cloud formation near the top of the simulated PBL, or horizontal advection. Latent heat release could be evaluated by calculating the change in water vapor mixing ratio corresponding to a positive change in cloud water mixing ratio. This would tell us approximately how much warming in the air is due to latent heating. Horizontal advection could be assessed by plotting horizontal wind with potential temperature and mixing ratio.

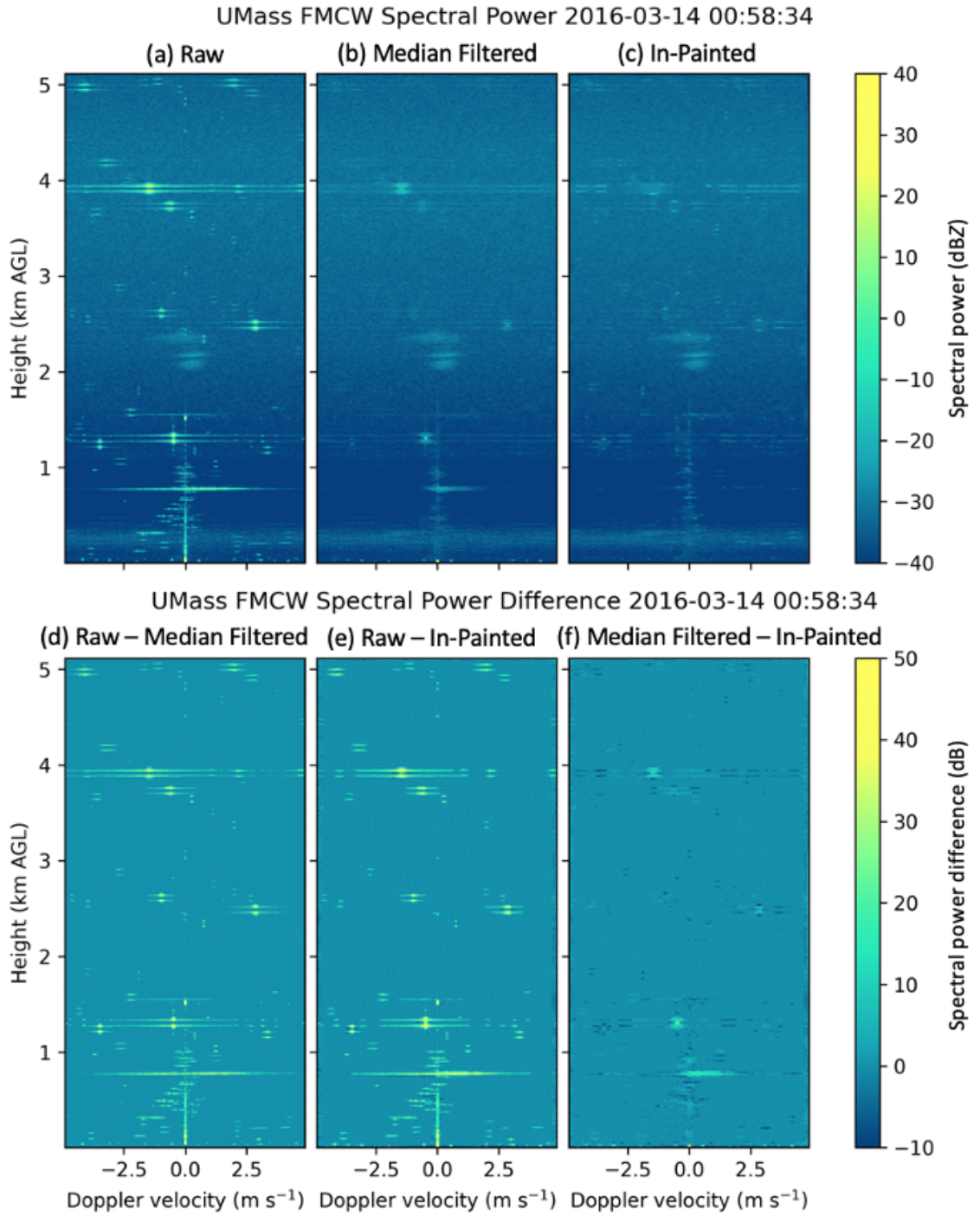


Figure 4.1. Spectral profiles (a-c) as in Fig. 3.2 and spectral power differences (d-f), but for a clear air case on 14 March 2016.

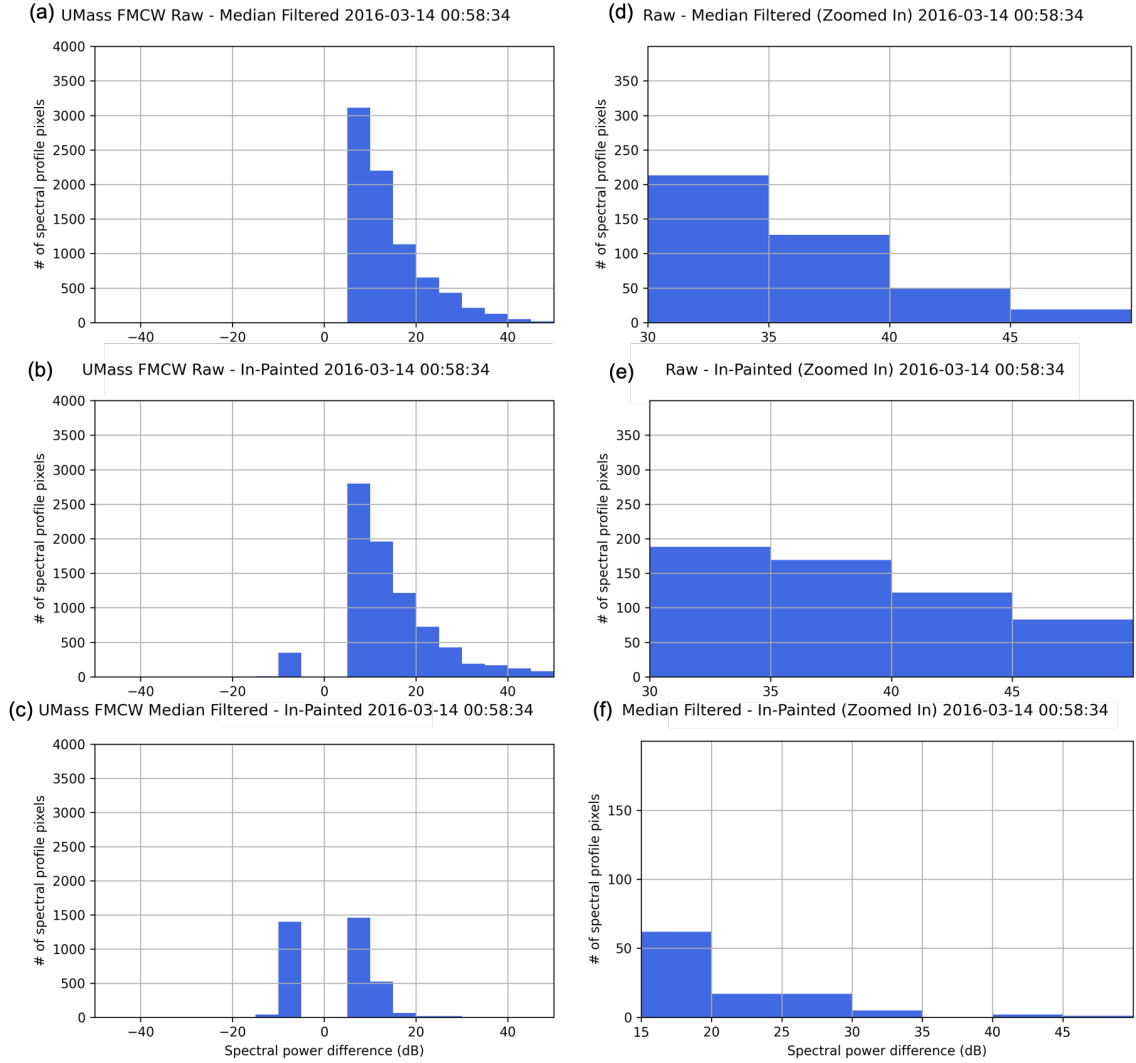


Figure 4.2. Spectral power difference histograms for a clear air case on 14 March 2016. Panels d-f zoom in on the right tail of the distribution.

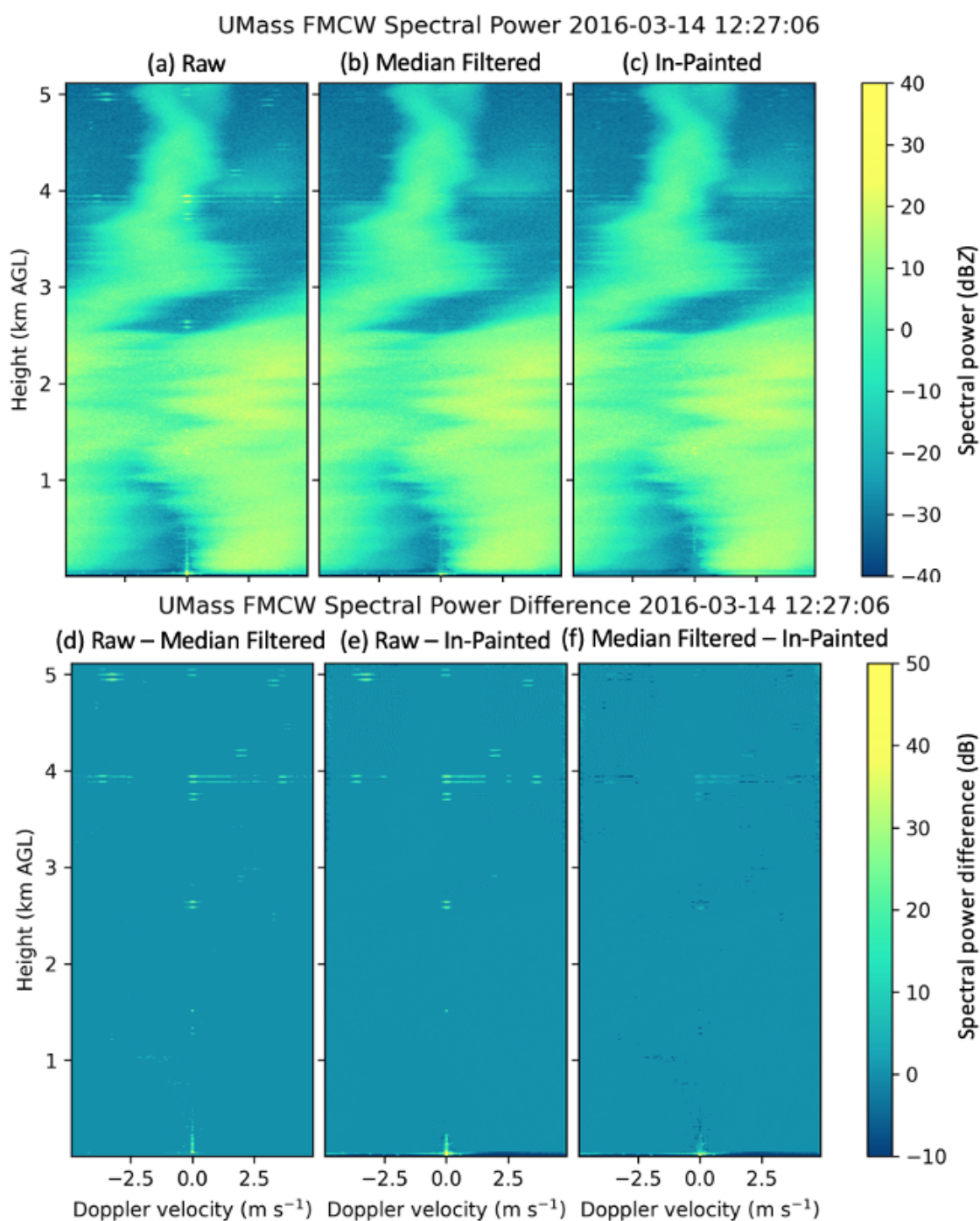


Figure 4.3. As in Fig. 4.1, but for precipitation on 14 March 2016.

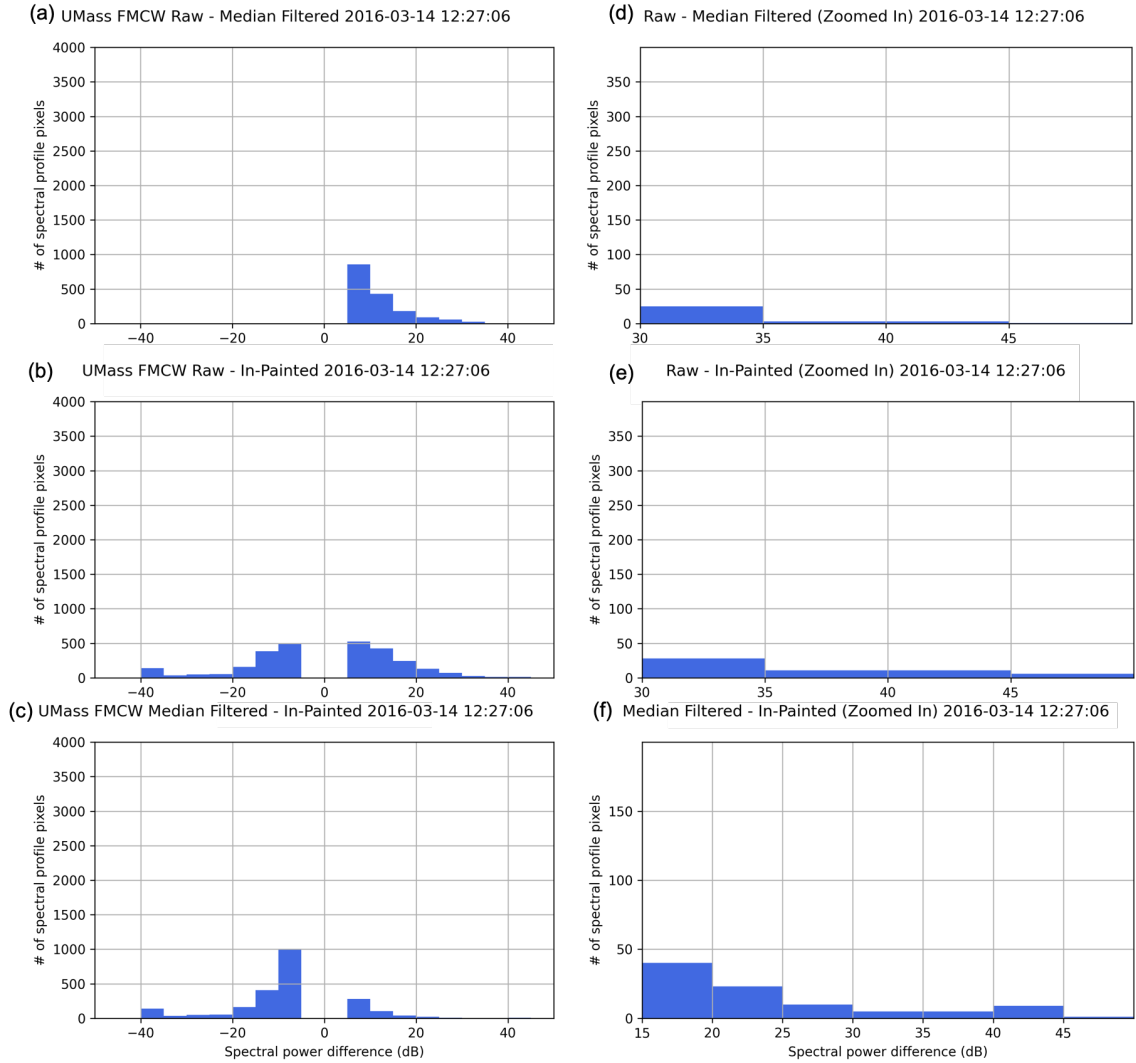


Figure 4.4. As in Fig. 4.2, but for precipitation on 14 March 2016.

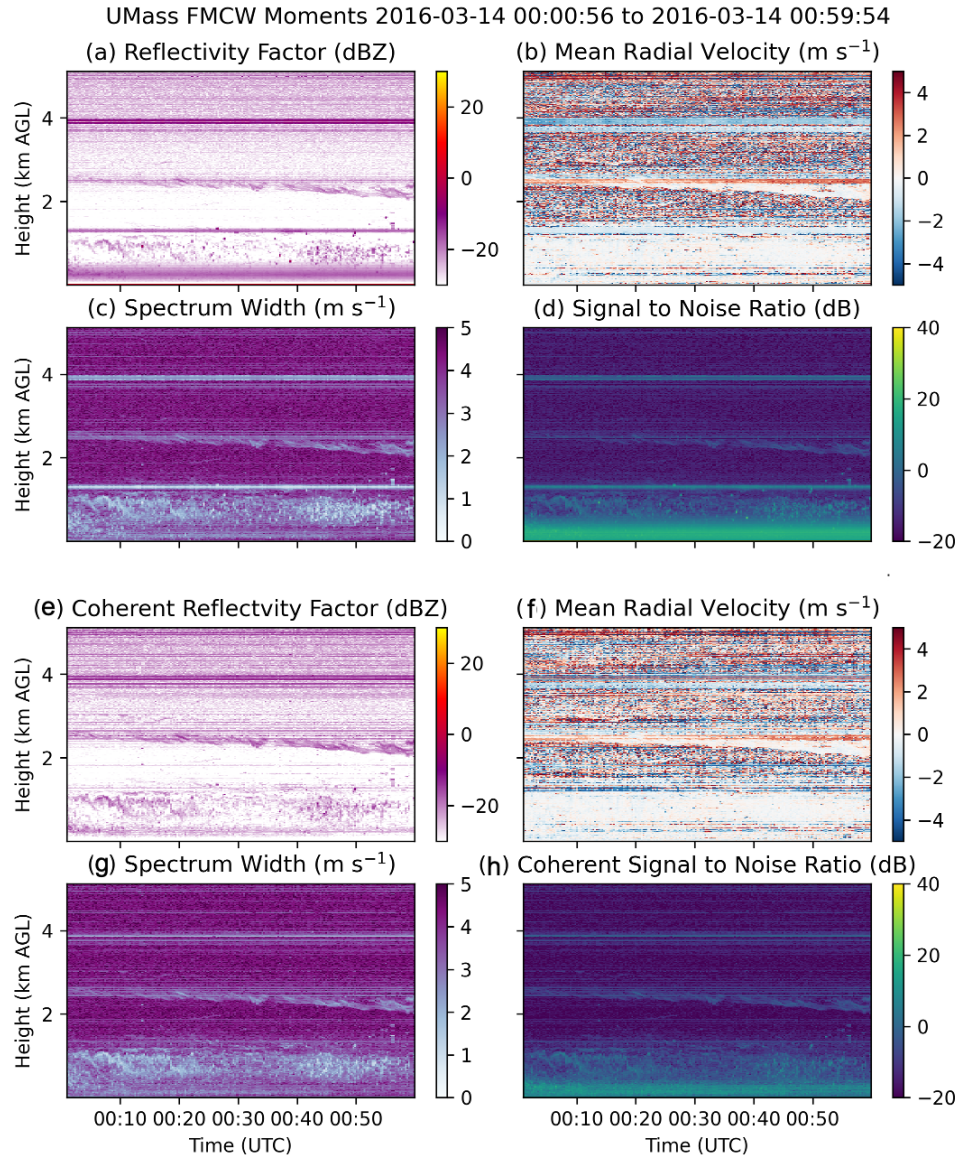


Figure 4.5. Clear air moments from 14 March 2016 that were calculated from the median filtered Doppler spectra (a-d) and in-painted Doppler spectra (e-h).

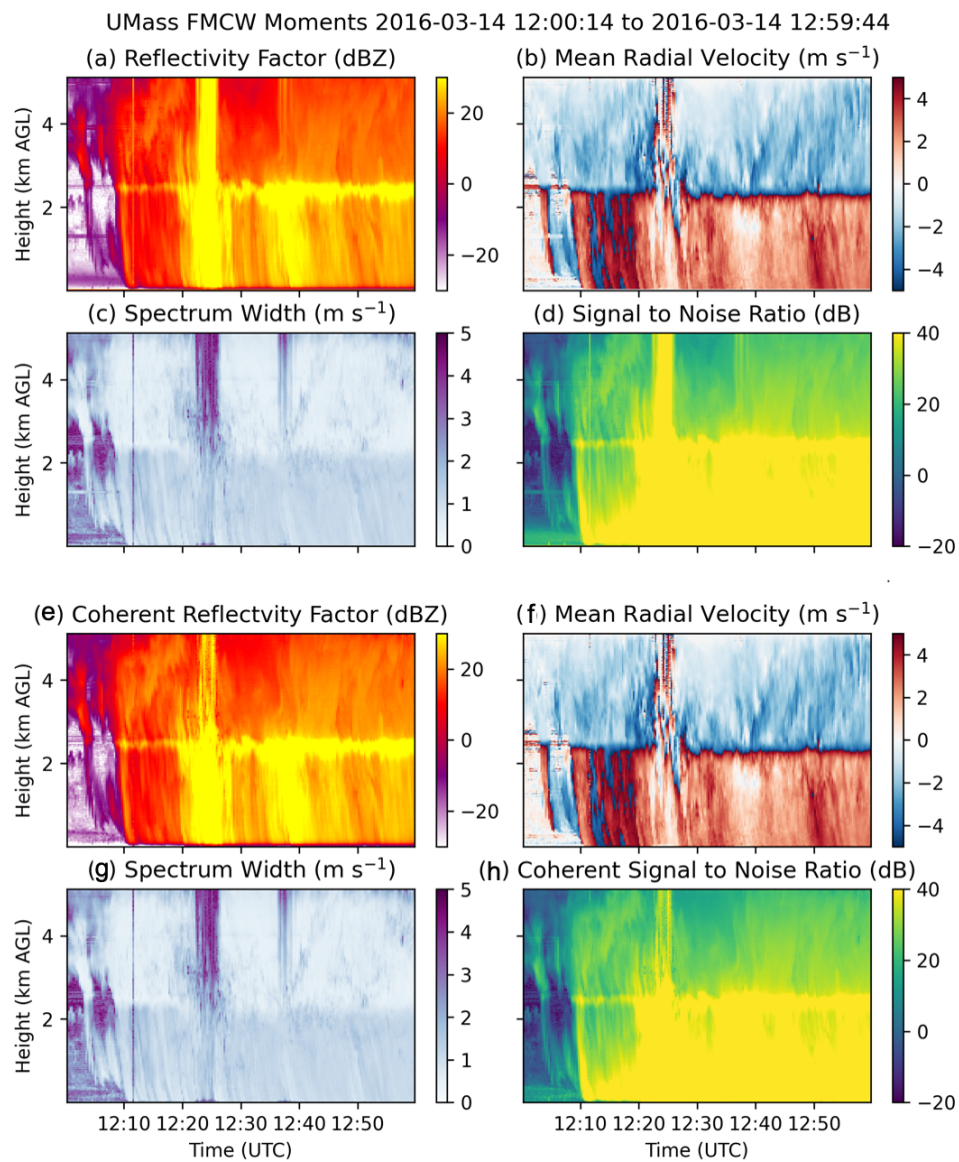


Figure 4.6. As in Fig. 4.5, but for precipitation on 14 March 2016.

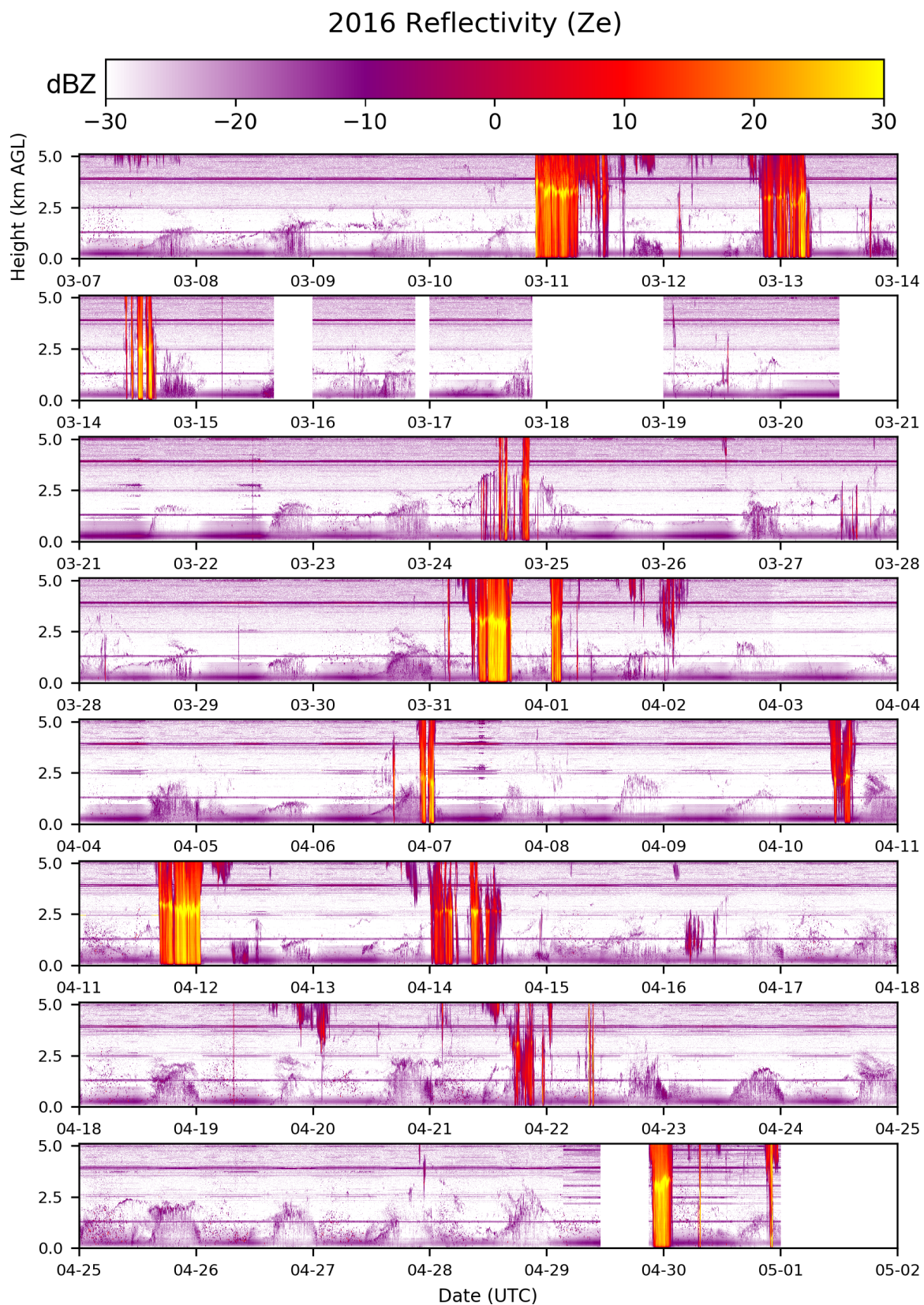


Figure 4.7. Reflectivity (in dBZ) from UMass FMCW observations taken during the 2016 VORTEX-Southeast field campaign. (From Tanamachi et al. 2019.)

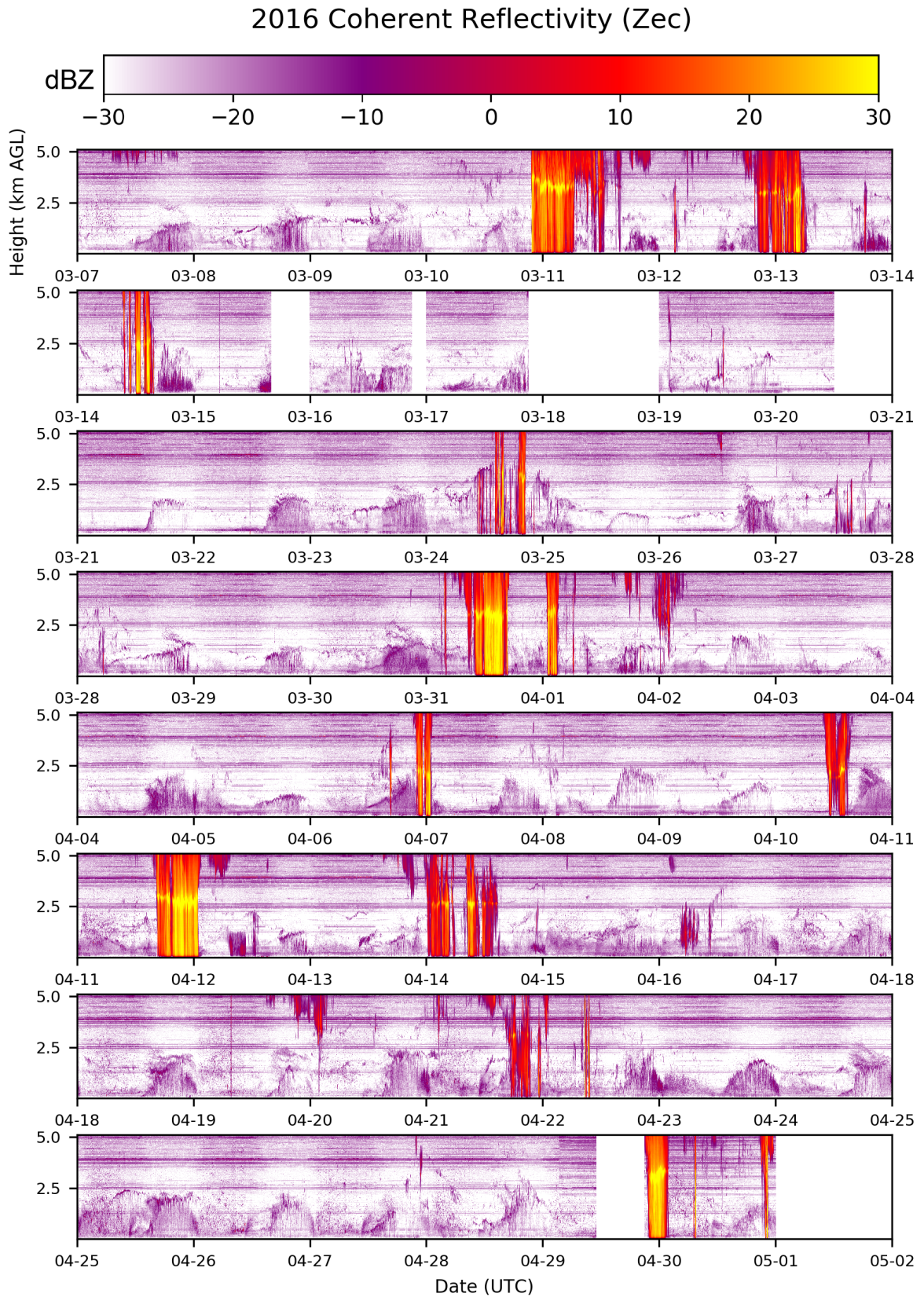


Figure 4.8. Coherent reflectivity (in dBZ) from UMass FMCW observations taken during the 2016 VORTEX-SE field campaign.

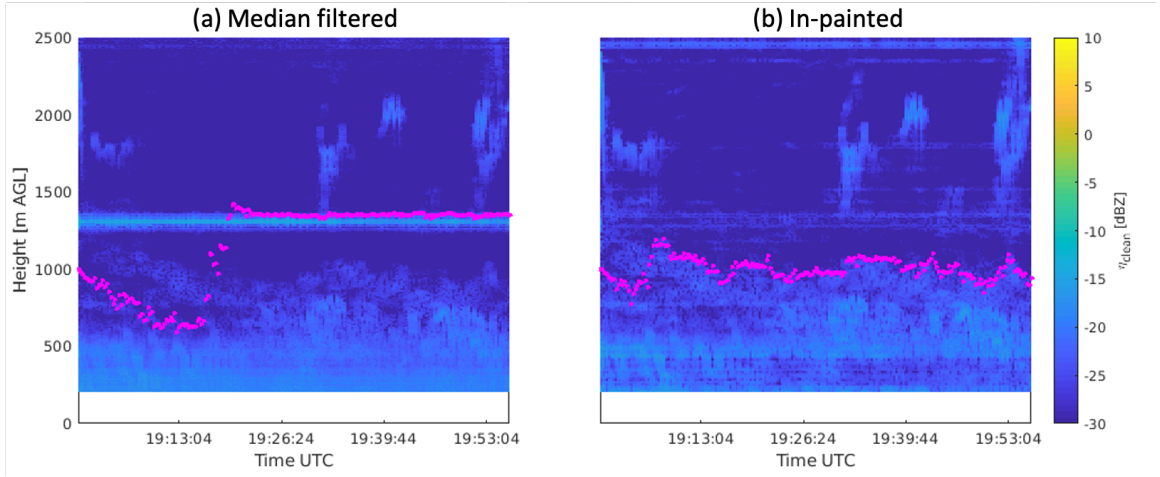


Figure 4.9. Boundary layer height detection algorithm for a clear-air CBL on 31 March 2016 for (a) median filtered reflectivity factor and (b) in-painted coherent reflectivity factor.

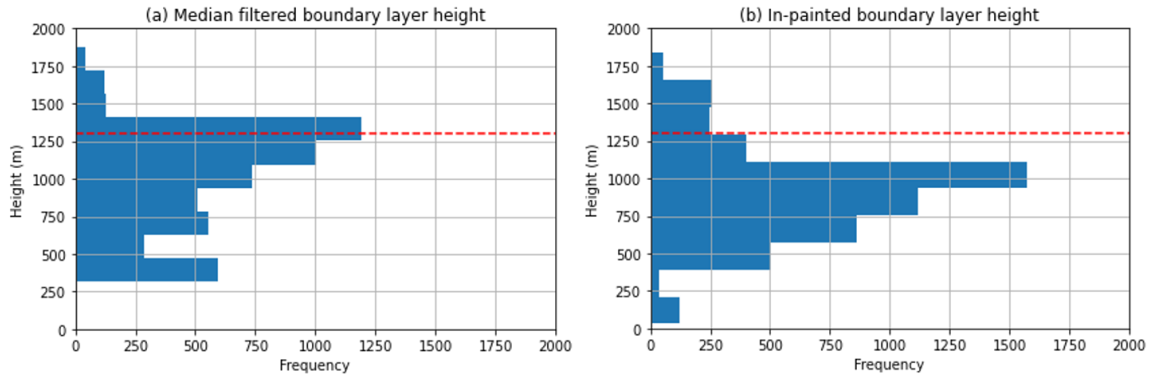


Figure 4.10. PBL height histograms for select clear air CBLs in March 2016 using (a) median filtered moments and (b) in-painted moments. The red line denotes the height of a known, persistent, high-power spur at 1.3 km (Figs. 1.1 and 4.7).

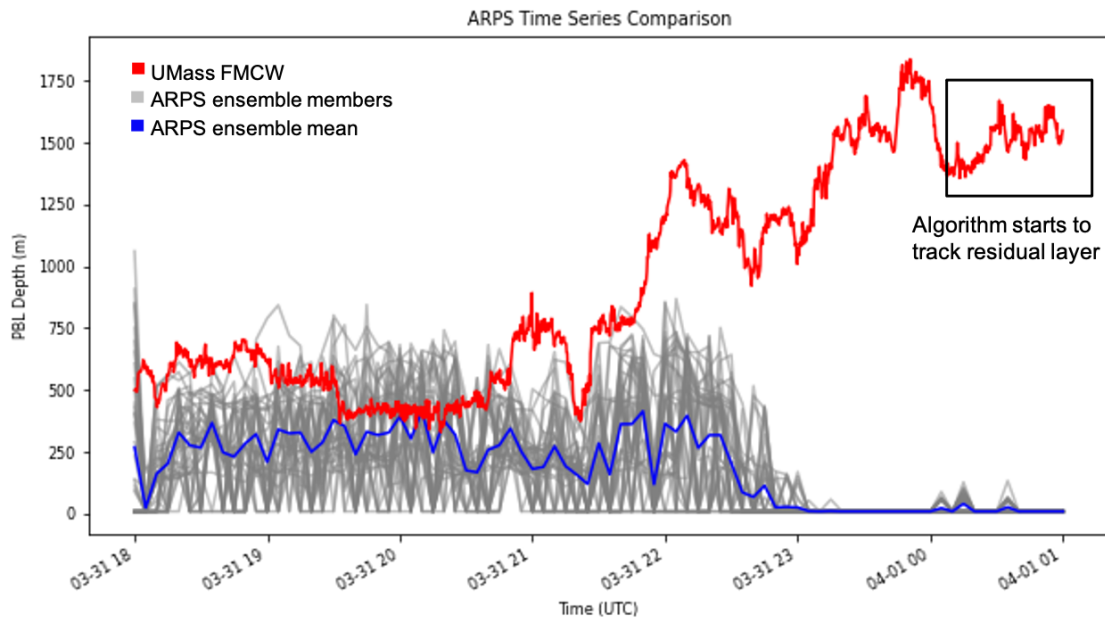


Figure 4.11. Time series of PBL depth from 1800 UTC 31 March 2016 to 0100 UTC 01 April 2016 for forecast PBL depth near Belle Mina, Alabama from the 40 ARPS ensemble members (gray), ARPS ensemble mean (blue), and UMass FMCW observations (red).

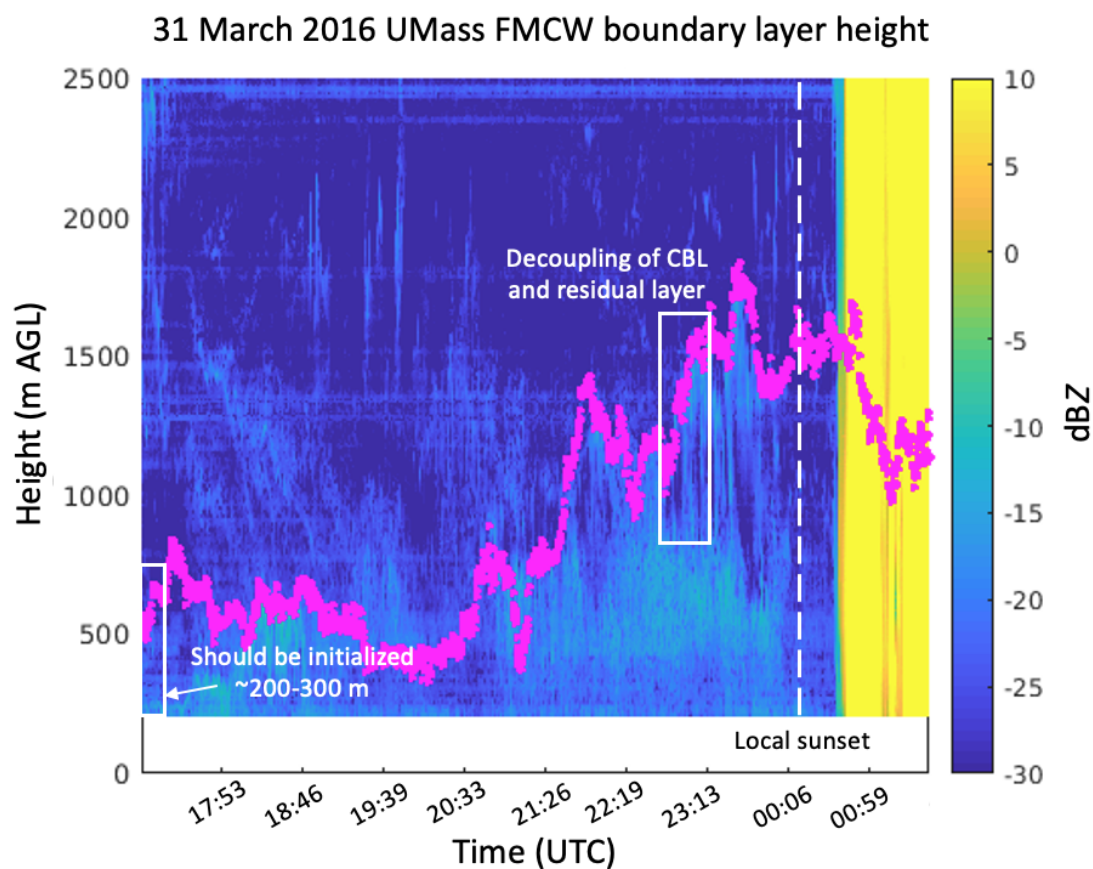


Figure 4.12. UMass FMCW boundary layer height retrievals (pink dots) from the Lange et al. (2015) algorithm for 1700 UTC to 0200 UTC 31 March 2016. Note that this time series is also plotted in red in Fig. 4.11.

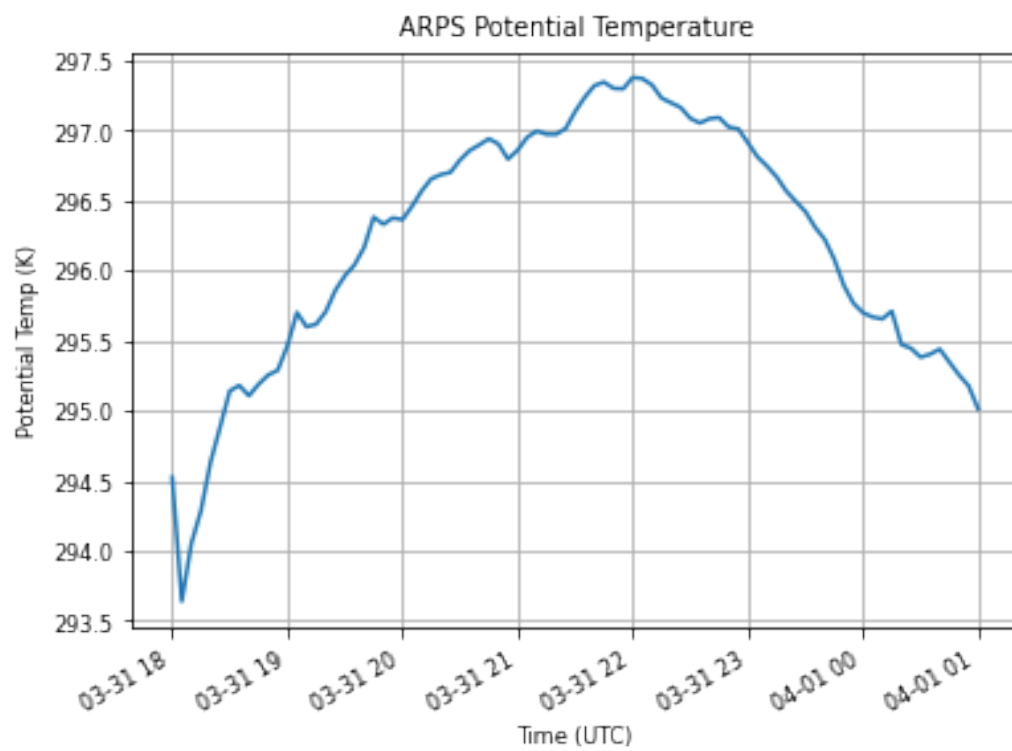


Figure 4.13. Time series of ensemble mean potential temperature from 1800 UTC 31 March 2016 to 0100 UTC 1 April 2016 near Belle Mina, Alabama from the ARPS model.

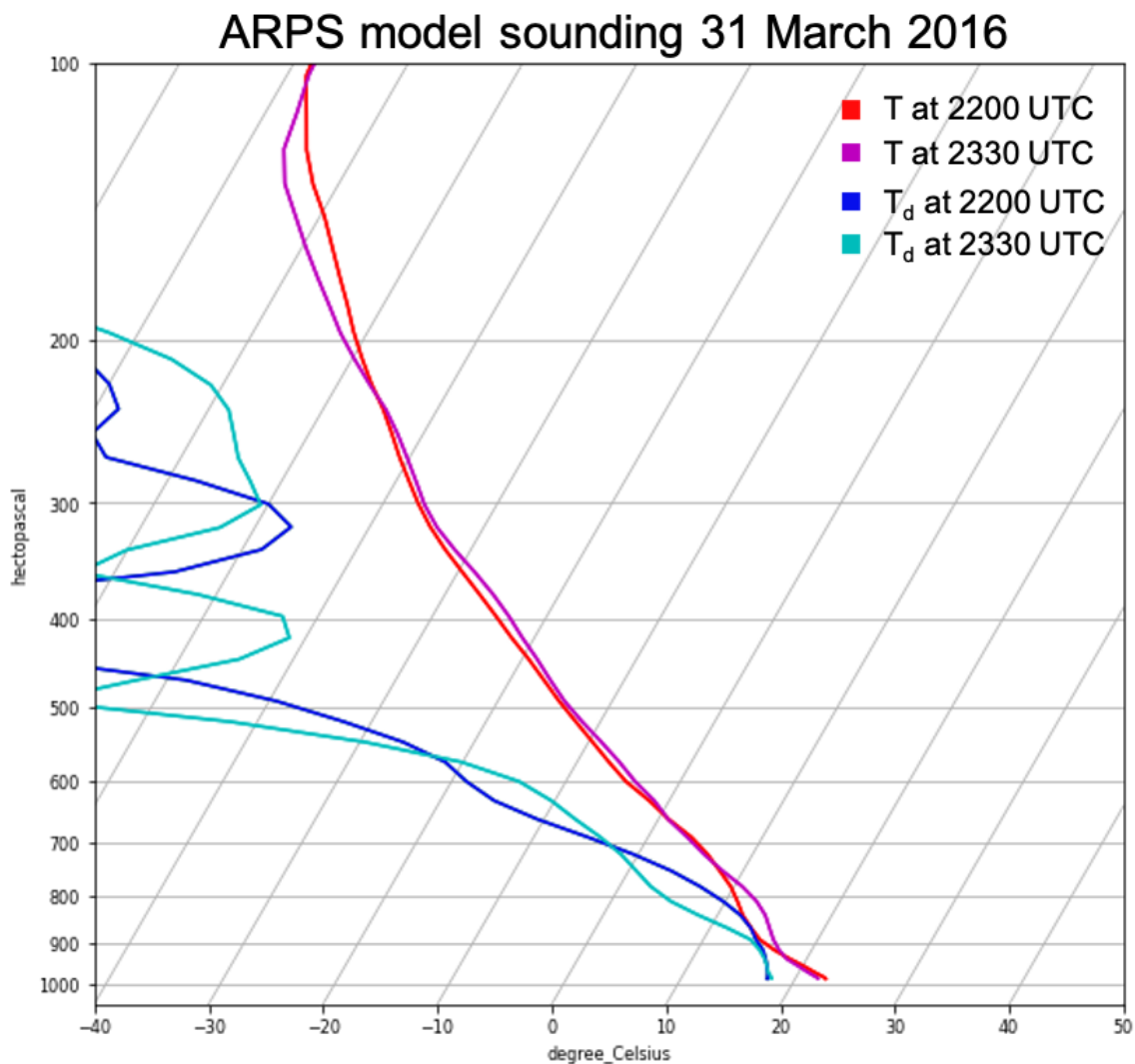


Figure 4.14. Skew-T, log p plot of ARPS model soundings (for ensemble member 1) before and after the boundary layer stabilization on 31 March 2016. Sounding values plotted are temperature (red line) and dew point temperature (blue line) at 2200 UTC, and temperature (magenta line) and dew point temperature (cyan line) at 2330 UTC. Note the warming and drying over the 900 hPa to 800 hPa layer between 2200 UTC and 2330 UTC.

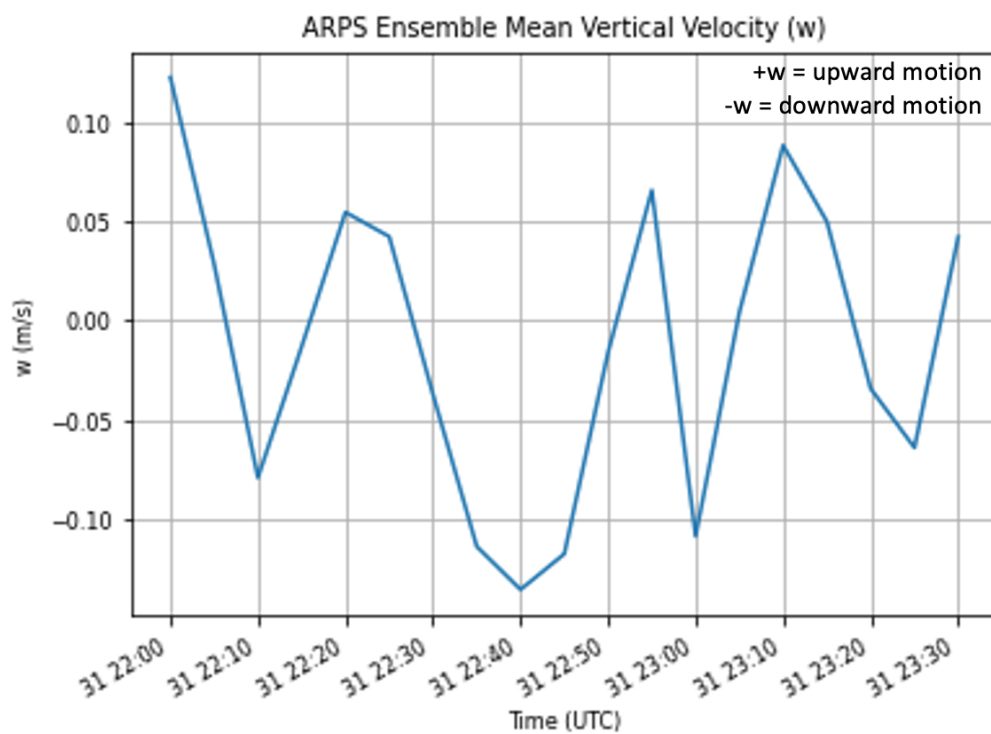


Figure 4.15. ARPS model ensemble mean vertical velocity (w) (blue line) from 2200 UTC to 2330 UTC 31 March 2016. Positive (negative) velocities correspond to upward (downward) motion.

5. CONCLUSIONS

We used a combination of two novel techniques, one from image processing and one from signal processing, to rectify a data quality issue in UMass FMCW spectra collected during the 2016 VORTEX-SE field campaign. To evaluate the extent of the improvement, spectral power differences are computed and analyzed, moments computed with median filtered and in-painted Doppler spectra are compared, and output from a boundary layer height detection algorithm is compared. Additionally, the observed boundary layer height derived from the UMass FMCW is compared to model forecast boundary layer height predicted by the ARPS mesoscale model for a single case study: 31 March 2016.

The Chan et al. (2016) in-painting method shows promising results when applied to Doppler spectra contaminated by sharp spectral peaks. The Chan et al. (2016) in-painting method does better than the previously applied median filter at removing the spurs from the Doppler spectra in both clear air and precipitation events. Owing to the restoration of the raw spectral structure in regions that are not in-painted, our method preserves more of the underlying Doppler spectral structure of the scatterers being sampled (Fig. 3.2c). These scatterers are mainly precipitation and bioscatterers, which tend to be smeared out in the median filter (Fig. 3.2b).

The radar moments were regenerated from the in-painted spectral profiles using a CP signal processing technique (Pazmany and Haimov 2018). In combination with the Chan et al. (2016) in-painting method, this type of signal processing removes most of the spurious reflectivity and SNR peaks resulting from the spectral peaks in both clear air and precipitation cases. Improvements in products further derived from these moments (i.e., automated CBL height detection) were demonstrated. Lastly, when comparing boundary layer height observations from the UMass FMCW with modeled PBL depth from ARPS, it is evident that convective scale models struggle with properly characterizing the boundary layer. Therefore, there is a need for supplemental boundary layer observations, such as those from profiling radars, to be assimilated into NWP models.

This work demonstrates the application of image processing and signal processing methods allowed for recovery of meteorological information from a contaminated data set. To the best of our knowledge, this study represents the first time these two methods have been applied together to Doppler spectra. Doppler spectra are often discarded from radar data because they are voluminous. (In this case, they consume 256 times as much disk space as the moments.) However, this study demonstrates that whenever possible/practical, Doppler spectra should be retained in case novel methods become available in the future that can aid in data recovery.

6. REFERENCES

- Agee, E., J. Larson, S. Childs, and A. Marmo, 2016: Spatial redistribution of U.S. tornado activity between 1954 and 2013. *J. Appl. Meteor. Climatol.*, **55**, 1681–1697.
- Anderson-Frey, A. K., Y. P. Richardson, A. R. Dean, R. L. Thompson, and B. T. Smith, 2019: Characteristics of tornado events and warnings in the southeastern United States. *Wea. Forecasting*, **34**, 1017–1034.
- Angevine, W. M., A. B. White, and S. K. Avery, 1994: Boundary-layer depth and entrainment zone characterization with a boundary-layer profiler. *Boundary-Layer Meteorol.*, **68**, 375–385.
- Ashley, W. S., 2007: Spatial and temporal analysis of tornado fatalities in the United States: 1880–2005. *Wea. Forecasting*, **22**, 1214–1228.
- _____, A. J. Krmenec, and R. Schwantes, 2008: Vulnerability due to nocturnal tornadoes. *Wea. Forecasting*, **23**, 795–807.
- Atlas, D., 1959: Meteorological “angel” echoes. *J. Meteor.*, **16**, 6–11.
- _____, 1960: Radar detection of the sea breeze. *J. Meteor.*, **17**, 244–258.
- _____, K. R. Hardy, and K. Naito, 1966: Optimizing the detection of clear-air turbulence. *J. Applied Meteor.*, **5**, 450–460.
- Austin, P. M., and A. C. Bemis, 1950: A quantitative study of the “bright band” in radar precipitation echoes, *J. of Atmos. Sci.*, **7**(2), 145–151.
- Bachmann, K., C. Keil, G. C. Craig, M. Weissmann, and C. A. Welzbacher, 2020: Predictability of deep convection in idealized and operational forecasts: Effects of radar data assimilation, orography, and synoptic weather regime. *Mon. Wea. Rev.*, **148**, 63–81.

- Banghoff, J. R., D. J. Stensrud, and M. R. Kumjian, 2018: Convective boundary layer depth estimation from S-band dual-polarization radar. *J. Atmos. Oceanic Technol.*, **35**, 1723–1733.
- Battan, L. J., 1959: *Radar Meteorology*. University of Chicago Press, 161 pp.
- Boyd, S., N. Parikh, E. Chu, B. Peleato, and J. Eckstein, 2011: Distributed optimization and statistical learning via the alternating direction method of multipliers. *Found. Trends Mach. Learn.*, **3**(1), 1–122.
- Branick, M., 1996: A comprehensive glossary of weather terms for storm spotters. *NOAA Tech, Mem.* NWS SR-145, 2nd ed., 49 pp.
- Brotzge, J., and S. Erickson, 2010: Tornadoes without NWS warning. *Wea. Forecasting*, **25**, 159–172.
- Burke, P. C., and D. M. Schultz, 2004: A 4-yr climatology of cold-season bow echoes over the continental United States. *Wea. Forecasting*, **19**, 1061–1074.
- Chadwick, R. B., K. P. Moran, R. G. Strauch, G. E. Morrison, and W. C. Campbell, 1976: Microwave radar wind measurements in the clear air. *Radio Sci.*, **11**, 795–802.
- Chan, S. H., X. Wang, and O. A. Elgendy, 2016: Plug-and-play admm for image restoration: Fixed-point convergence and applications. *IEEE Transactions on Computational Imaging*, **3**(1), 84–98.
- Cohen, A. E., S. M. Cavallo, M. C. Coniglio, and H. E. Brooks, 2015: A review of planetary boundary layer parameterization schemes and their sensitivity in simulating southeastern U.S. cold season severe weather environments. *Wea. Forecasting*, **30**, 591–612.

- _____, _____, _____, _____, and I. L. Jirak, 2017: Evaluation of multiple planetary boundary layer parameterization schemes in Southeast U.S. cold season severe thunderstorm environments. *Wea. Forecasting*, **32**, 1857–1884.
- Cohn, S. A., and W. M. Angevine, 2000: Boundary layer height and entrainment zone thickness measured by lidars and wind-profiling radars. *J. Appl. Meteor.*, **39**, 1233–1247.
- Davis, J. M., and M. D. Parker, 2014: Radar climatology of tornadic and nontornadic vortices in high-shear, low-CAPE environments in the mid-Atlantic and southeastern United States. *Wea. Forecasting*, **29**, 828–853.
- Dixon, P. G., A. E. Mercer, J. Choi, and J. S. Allen, 2011: Tornado risk analysis: Is Dixie Alley an extension of Tornado Alley?. *Bull. Amer. Meteor. Soc.*, **92**, 433–441.
- Doviak, R. J., and D. S. Zrnić, 1993: *Doppler radar and weather observations*. Dover Publications Inc. 562 pp.
- Eaton, F. D., S. A. McLaughlin, and J. R. Hines, 1995: A new frequency-modulated continuous wave radar for studying planetary boundary layer morphology. *Radio Sci.*, **30**, 75–88.
- Elmore, K. L., P. L. Heinselman, and D. J. Stensrud, 2012: Using WSR-88D data and insolation estimates to determine convective boundary layer depth. *J. Atmos. Oceanic Technol.*, **29**, 581–588.
- Evensen, G., 1994: Sequential data assimilation with a nonlinear quasi-geostrophic model using Monte Carlo methods to forecast error statistics. *J. Geophys. Res.*, **99**, 10143–10162.

- Evensen, G., 2003: The ensemble Kalman filter: Theoretical formulation and practical implementation. *Ocean Dyn.*, **53**, 343–367.
- Fabry, F., and I. Zawadzki, 1995: Long-term radar observations of the melting layer of precipitation and their interpretation. *J. Atmos. Sci.*, **52**, 838–851.
- Frasier, S., and J. Waldinger, 2016: UMass S-band FMCW profiling radar data, in netCDF format. Version 1.0. UCAR/NCAR - Earth Observing Laboratory. [Available online at <https://data.eol.ucar.edu/dataset/527.016>.]
- Li, F., and D. R. Chavas, 2021: Midlatitude continental CAPE is predictable from large-scale environmental parameters. *Geophys. Res. Letters*, **48**.
- Gage, K. S., and B. B. Balsley, 1978: Doppler radar probing of the clear atmosphere. *Bull. Amer. Meteor. Soc.*, **59**, 1074–1094.
- Garratt, J. R., 1992: *The Atmospheric Boundary Layer*. Cambridge University Press, 316 pp.
- Gensini, V. A., and H. E. Brooks, 2018: Spatial trends in United States tornado frequency. *npj Clim Atmos Sci* **1**, 38.
- Gossard, E. E., 1990: Radar research on the atmospheric boundary layer. *Radar in Meteorology: Battan Memorial and 40th Anniversary Radar Meteorology Conference*, D. Atlas, Ed., American Meteorological Society, 477–527.
- Grimsdell, A. W., and W. M. Angevine, 1998: Convective boundary layer height measurement with wind profilers and comparison to cloud base. *J. Atmos. Oceanic Technol.*, **15**, 1331–1338.

- Guyer, J. L., D. A. Imy, A. Kis, and K. Venable, 2006: Cool season significant (F2-F5) tornadoes in the Gulf Coast states. Preprints, *23rd Conf. on Severe Local Storms*, St. Louis, MO, Amer. Meteor. Soc., 4.2. [Available online at <https://ams.confex.com/ams/pdfpapers/115320.pdf>.]
- _____, and A. R. Dean, 2010: Tornadoes within weak CAPE environments across the continental United States. Preprints, *25th Conf. on Severe Local Storms*, Denver, CO, Amer. Meteor. Soc., 1.5. [Available online at https://ams.confex.com/ams/25SLS/techprogram/paper_175725.htm]
- Hardy, K. R., and I. Katz, 1969: Probing the clear atmosphere with high power, high resolution radars. *Proc. IEEE*, **57**, 468–480.
- _____, D. Atlas, and K. M. Glover, 1966: Multiwavelength backscatter from the clear atmosphere. *J. Geophys. Res.*, **71**, 1537–1552.
- Hegazy, A., M. Mosaad, and A. M. Hassan, 2016: FMCW software defined radar for range and speed estimation. 10.13140/RG.2.1.2116.3761.
- Heinselman, P. L., P. L. Spencer, K. L. Elmore, D. J. Stensrud, R. M. Hluchan, and P. C. Burke, 2009: Radar reflectivity–based estimates of mixed layer depth. *J. Atmos. Oceanic Technol.*, **26**, 229–239.
- Houtekamer, P. L., and H. L. Mitchell, 1998: Data assimilation using an ensemble Kalman filter technique. *Mon. Wea. Rev.*, **126**, 796–811.
- _____, _____, G. Pellerin, M. Buehner, M. Charron, L. Spacek, and B. Hansen, 2005: Atmospheric data assimilation with an ensemble Kalman filter: Results with real observations. *Mon. Wea. Rev.*, **133**, 604–620.

- Ince, T., A. L. Pazmany, and S. J. Frasier, 2000: High resolution profiling of the atmospheric boundary layer. IGARSS 2000: IEEE 2000 Int. Geoscience and Remote Sensing Symp., Honolulu, HI, IEEE, 209–211.
- _____, S. J. Frasier, A. Muschinski, and A. L. Pazmany, 2003: An S-band frequency-modulated continuous-wave boundary layer profiler: Description and initial results. *Radio Sci.*, **38**(4), 1072.
- Johns, R. H., and C. A. Doswell III, 1992: Severe local storms forecasting. *Wea. and Forecasting*, **7**(4), 588–612.
- Johnson, K.W., J. Bauer, G. A. Ricciardi, K. K. Droegemeier, and M. Xue, 1994: Distributed processing of a regional prediction model. *Mon. Wea. Rev.*, **122**, 2558–2572.
- Jung, Y., G. Zhang, and M. Xue, 2008: Assimilation of simulated polarimetric radar data for a convective storm using the ensemble Kalman filter. Part I: Observation operators for reflectivity and polarimetric variables. *Mon. Wea. Rev.*, **136**, 2228–2245.
- Kalnay, E., 2003: *Atmospheric modeling, data assimilation, and predictability*. Cambridge University Press. 369 pp.
- Kis, A. K., and J. M. Straka, 2010: Nocturnal tornado climatology. *Wea. Forecasting*, **25**, 545–561.
- Koch, S., 2016: VORTEX-SE: Program and activities. *28th Conf. on Severe Local Storms*, Portland, Oregon, Amer. Meteor. Soc., 3.1. [Available online at <https://ams.confex.com/ams/28SLS/webprogram/Paper300782.html>.]

- Kropfli, R. A., I. Katz, T. G. Konrad, and E. B. Dobson, 1968: Simultaneous radar reflectivity measurements and refractive index spectra in the clear atmosphere. *Radio Sci.*, **68D**, 895–901.
- LaFleur, A. T., R. Tanamachi, D. T. Dawson, S. J. Frasier, J. Waldinger, and D. D. Turner, 2018: The role of direct insolation and near-surface moisture advection in the recovery of CAPE on 31 March 2016 during VORTEX-Southeast. Preprints, *29th Conf. on Severe Local Storms*, Stowe, VT, Amer. Meteor. Soc., 100. [Available online at <https://ams.confex.com/ams/29SLS/webprogram/Paper348445.html>.]
- Lane, J. A., 1969: Radar echoes from clear air in relation to refractive-index variations in the troposphere. *Proc. IEEE*, **116**, 1656–1660.
- Lange, D., F. Rocadenbosch, J. Tiana-Alsina, and S. Frasier, 2015: Atmospheric boundary layer height estimation using a Kalman filter and a frequency-modulated continuous-wave radar. *IEEE Transactions on Geoscience and Remote Sensing*, **53**(6), 3338–3349.
- NOAA, 2007: Enhanced fujita tornado damage scale. [Available online at <https://www.spc.noaa.gov/faq/tornado/ef-scale.html>.]
- NWS Storm Prediction Center, 2016: Mesoscale Discussion #311. [Available online at <https://www.spc.noaa.gov/products/md/2016/md0311.html>.]
- NWS Storm Prediction Center, 2016: Tornado Watch #72. [Available online at <https://www.spc.noaa.gov/products/watch/2016/ww0072.html>.]
- Markowski, P. M., and Y. P. Richardson, 2010: *Mesoscale meteorology in midlatitudes*. Wiley-Blackwell, 407 pp.

- Marquis, J., Y. Richardson, P. Markowski, D. Dowell, J. Wurman, K. Kosiba, P. Robinson, and G. Romine, 2014: An investigation of the Goshen County, Wyoming, tornadic supercell of 5 June 2009 using EnKF assimilation of mobile mesonet and radar observations collected during VORTEX2. Part I: Experiment design and verification of the EnKF analyses. *Mon. Wea. Rev.*, **142**, 530–554.
- Melnikov, V., and D. S. Zrnić, 2017: Observations of convective thermals with weather radar. *J. Atmos. Oceanic Technol.*, **34**, 1585–1590.
- Ottersten, H., 1969: Atmospheric structure and radar backscattering in clear air. *Radio Sci.*, **(4)12**, 1179–1193.
- Pazmany, A. L., and S. J. Haimov, 2018: Coherent power measurements with a compact airborne Ka-band precipitation radar. *J. Atmos. Oceanic Technol.*, **35**(1), 3–20.
- Przybylinski, R.W., 1995: The bow echo: Observations, numerical simulations, and severe weather detection methods. *Wea. Forecasting*, **10**, 203–218.
- Ralph, F. M., 1995: Using radar-measured radial vertical velocities to distinguish precipitation scattering from clear-air scattering. *J. Atmos. Oceanic Technol.*, **12**(2), 257–267.
- Rauber, R. M., and S. W. Nesbitt, 2018: *Radar meteorology: A first course*. John Wiley & Sons. 461 pp.
- Rasmussen, E. N., 2015: VORTEX-Southeast program overview. National Severe Storms Laboratory Rep., 36 pp.
- _____, and S. Koch, 2016: VORTEX-SE: Lessons learned and early results. *28th Conf. on Severe Local Storms*, Portland, Oregon, Amer. Meteor. Soc., 3.2, [Available online at <https://ams.confex.com/ams/28SLS/webprogram/Paper301782.html>.]

- Richter, J. H., 1969: High resolution tropospheric radar sounding. *Radio Sci*, **4**(12), 1261–1268.
- Schneider, R. S., A. R. Dean, S. J. Weiss, and P. D. Bothwell, 2006: Analysis of estimated environments for 2004 and 2005 severe convective storm reports. Preprints, *23rd Conf. on Severe Local Storms*, St. Louis, MO, Amer. Meteor. Soc., 3.5. [Available online at <https://ams.confex.com/ams/pdfpapers/115246.pdf>.]
- Sherburn, K. D., and M. D. Parker, 2014: Climatology and ingredients of significant severe convection in high-shear, low-CAPE environments. *Wea. Forecasting*, **29**, 854–877.
- Simmons, K. M., and D. Sutter, 2005: WSR-88D radar, tornado warnings, and tornado casualties. *Wea. Forecasting*, **20**, 301–310.
- Smith, B. T., J. L. Guyer, and A. R. Dean, 2008: The climatology, convective mode, and mesoscale environment of cool season severe thunderstorms in the Ohio and Tennessee Valleys, 1995–2006. Preprints, *24th Conf. on Severe Local Storms*, Savannah, GA, Amer. Meteor. Soc., 13B.7. [Available online at <https://ams.confex.com/ams/pdfpapers/141968.pdf>.]
- Snook, N., M. Xue, and Y. Jung, 2012: Ensemble probabilistic forecasts of a tornadic mesoscale convective system from ensemble Kalman filter analyses using WSR-88D and CASA radar data. *Mon. Wea. Rev.*, **140**, 2126–2146.
- _____, _____, and _____, 2015: Multiscale EnKF assimilation of radar and conventional observations and ensemble forecasting for a tornadic mesoscale convective system. *Mon. Wea. Rev.*, **143**, 1035–1057.

- Stensrud, D. J., and S. J. Weiss, 2002: Mesoscale model ensemble forecasts of the 3 May 1999 tornado outbreak. *Wea. Forecasting*, **17**, 526–543.
- Strader, S. M., and W. S. Ashley, 2018: Finescale assessment of mobile home tornado vulnerability in the central and southeast United States. *Wea. Climate Soc.*, **10**, 797–812.
- _____, _____, T. J. Pingel, and A. J. Krmenec, 2017: Observed and projected changes in United States tornado exposure. *Wea. Climate Soc.*, **9**, 109–123.
- Stull, R. B.; 1988: An introduction to boundary layer meteorology. Kluwer Academic Publishers, Dordrecht, Boston and London, 666 pp.
- _____, 2017: Practical meteorology: An algebra-based survey of atmospheric science. 926 pp.
- Supinie, T. A., Y. Jung, M. Xue, D. J. Stensrud, M. M. French, and H. B. Bluestein, 2016: Impact of VORTEX2 observations on analyses and forecasts of the 5 June 2009 Goshen County, Wyoming, supercell. *Mon. Wea. Rev.*, **144**, 429–449.
- Talagrand, O., 1997: Assimilation of observations, an introduction. *J. Met. Soc. Japan*, **75**(1B), 191–209.
- Tanamachi, R. L., S. J. Frasier, J. Waldinger, A. LaFleur, D. D. Turner, and F. Rocadenbosch, 2019: Progress toward characterization of the atmospheric boundary layer over northern Alabama using observations by a vertically pointing, S-band profiling radar during VORTEX-Southeast. *J. Atmos. Oceanic Technol.*, **36**, 2221–2246.

- _____, L. J. Wicker, D. C. Dowell, H. B. Bluestein, D. T. Dawson, and M. Xue, 2013: EnKF assimilation of high-resolution, mobile Doppler radar data of the 4 May 2007 Greensburg, Kansas, supercell into a numerical cloud model. *Mon. Wea. Rev.*, **141**, 625–648.
- Thompson, R. L., R. Edwards, and C.M. Mead, 2004: An update to the supercell composite and significant tornado parameters. Preprints, *22nd Conf. Severe Local Storms*, Hyannis, MA, Amer. Meteor. Soc., P8.1. [Available online at <https://ams.confex.com/ams/11aram22sls/webprogram/Paper82100.html>.]
- Ulaby, F. T., R. K. Moore, and A. K. Fung, 1982: Radar remote sensing and surface scattering and emission theory. vol. ii, microwave remote sensing: Active and passive. Addison-Wesley Publishing Co., 634 pp.
- Wagner, T. J., P. M. Klein, and D. D. Turner, 2019: A new generation of ground-based mobile platforms for active and passive profiling of the boundary layer. *Bull. Amer. Meteor. Soc.*, **100**, 137–153.
- Waldinger, J., 2018: Improvements to the UMASS S-band FM-CW vertical wind profiling radar: System performance and data analysis. M.S.E.C.E. thesis, University of Massachusetts Amherst.
- Waldinger J., T. Hartley, W. Heberling, S. Frasier, and R. Tanamachi, 2017: S-band FMCW boundary layer profiler: System upgrades and results. *IEEE International Geoscience and Remote Sensing Symposium (IGARSS)*, Fort Worth, TX, 4526–4529.
- Wolff, C., 1998: Radartutorial.eu (English version). [Available online at <https://www.radartutorial.eu/index.en.html>.]

- Wyngaard, J. C., and M. A. LeMone, 1980: Behavior of the refractive index structure parameter in the entraining convective boundary layer. *J. Atmos. Sci.*, **37**, 1573–1585.
- Xiao, Q., and J. Sun, 2007: Multiple-radar data assimilation and short-range quantitative precipitation forecasting of a squall line observed during IHOP_2002. *Mon. Wea. Rev.*, **135**, 3381–3404.
- Xue, M., K. K. Droegemeier, and V. Wong, 2000: The Advanced Regional Prediction System (ARPS)—A multi-scale nonhydrostatic atmospheric simulation and prediction tool. Part I: Model dynamics and verification. *Meteor. Atmos. Phys.*, **75**, 161–193.
- _____, M. Tong, and K. K. Droegemeier, 2005: Impact of radar configuration and scan strategy on assimilation of radar data using ensemble Kalman filter. Preprints, *Ninth Symp. on Integrated Observing and Assimilation Systems for the Atmosphere, Oceans, and Land Surface*, San Diego, CA, Amer. Meteor. Soc., 9.3. [Available online at https://ams.confex.com/ams/Annual2005/techprogram/paper_86681.htm]